A numerical study of the effect of nozzle diameter on Diesel combustion ignition and flame stabilization

Author names

J.M. Desantes, J.M. García-Oliver, R. Novella, L. Pachano

CMT-Motores Térmicos, Universitat Politècnica de València, Valencia 46022, Spain

Abstract

The role of nozzle diameter on Diesel combustion is studied by performing CFD calculations of Spray A and Spray D from the Engine Combustion Network (ECN). These are well-characterized single-hole sprays in a quiescent environment chamber with thermodynamic conditions representative of modern Diesel engines. First, the inert spray evolution is described with the inclusion of the concept of mixing trajectories and local residence time into the analysis. Such concepts enable the quantification of the mixing rate, showing that it decreases with the increase in nozzle diameter. In a second step, the reacting spray evolution is studied focusing on the local heat release rate distribution during the auto-ignition sequence and the quasi-steady state. The capability of a well-mixed based and a flamelet based combustion model to predict Diesel combustion is also assessed. On the one hand, results show that turbulence-chemistry interaction has a profound effect on the description of the reacting spray evolution. On the other hand, the mixing rate, characterized in terms of the local residence time, drives the main changes introduced by the increase of the nozzle diameter when comparing Spray A and Spray D.

Keywords

Diesel spray, nozzle diameter, residence time, well-mixed, flamelet

1 Introduction

Fuel and thermal efficiency in internal combustion engines (ICE) relying on compression ignition (CI) are still attractive features for industries focused on diverse sectors such as automotive, road transportation and marine applications. Despite its operational advantages, pollutant emissions from CI combustion systems can potentially deteriorate local air quality and therefore human health. As a consequence, the latest advancements in CI combustion systems are driven by stricter regulations predominantly oriented to reduce permissible limits for particulate matter emissions. The challenge of improving the understanding of turbulent combustion, hence pollutant formation, remains crucial for the development and enhancement of CI combustion systems.

In particular, the nozzle size is a geometrical parameter that brings about differences in combustion behavior between light and heavy-duty engines. From the experimental point of view, changes in nozzle orifice diameter have been observed to greatly influence the amount of soot formed in Diesel flames. In this direction, Pickett and Siebers[1,2] conducted experiments using a single-hole nozzle in a constant-volume vessel with pressure and temperature conditions representative of direct injection (DI) Diesel engines. Authors concluded that under the same operating condition decreasing nozzle orifice diameter increased the air-entrainment rate (relative to the amount of fuel injected) upstream of the lift-off length (LOL). As more air is entrained the average equivalence ratio at the LOL location (ϕ_{LOL}) decreases. The authors found that the decrease in ϕ_{LOL} at the flame base also decreases the total amount of soot formed, proving the feasibility of mitigating soot emissions by decreasing the nozzle orifice diameter. Chengjun et al.[3] also observed the influence of the nozzle orifice diameter on the average value of ϕ_{LOL}, hence on soot formation, in single-hole Diesel sprays in a constant-pressure vessel. The authors also found that a reduced value of ϕ_{LOL} induced by the reduction of nozzle orifice diameter caused an increase in the OH zone thickness (based on OH* chemiluminescence imaging) and a consequent reduction of the maximum soot volume fraction zone. Pastor et al.[4] approached the study of different nozzle diameters based on the analysis of spray dynamics and mixing field in a constant-pressure vessel. Experiments were carried-out to measure spray tip penetration, LOL and ignition delay time (ID). Under the same operating conditions, differences in results among different nozzles were explained by spray dynamics (in agreement with momentum-driven gas jets theory) and the state of the mixing field prior to the start of combustion retrieved with a 1D model.

It is worth mentioning that the study of reacting sprays with different nozzle orifice diameters is not limited to fundamental studies as the aforementioned cases. It can also be extended to applications in which two different nozzles are used for pilot and main injections as in the case of marine engines. In that field, Ishibashi and Tsuru[5] studied Diesel spray and gas injection combustion in a rapid compression machine with a 160 μm nozzle for a pilot injection and a 500 μm for a main injection.

From the simulation point of view Pang et al.[6] conducted a numerical study on reacting sprays in a combustion vessel with nozzle orifice diameters of 100 μm, 180 μm and 363 μm. Results are in line with experimental observations with shorter LOL and average leaner mixtures at this location with smaller nozzles. As fewer computational studies comparing different nozzle diameters are available, the present work aims to use computational fluid dynamics (CFD) to study the role that the nozzle orifice diameter plays on Diesel combustion. The Engine Combustion Network (ENC)[7] Spray A will be used as the main reference case for this work. The Spray A experiment, a single-hole nozzle injecting into a quiescent environment with thermodynamic conditions representative of CI engines, has allowed the development of an extensive database of experimental results.[8–13] On the simulation side, the single-hole nozzle experiment has enabled the comprehensive validation of the two-phase turbulent spray using both Lagrangian-Eulerian[14–17] and Eulerian[18,19] approaches.

Within the scope of the present work, different approaches to model the sub-grid flame structure will be also evaluated. Results from a detailed chemistry solver based on the well-mixed (WM) assumption and results from a model based on the flamelet assumption are compared. These two different approaches for combustion modeling allow to assess the importance of turbulence-chemistry interaction (TCI). Comparisons of such combustion models have been reported in the literature assessing the capabilities of well-mixed based models and a representative interactive linear eddy model,[20] transported probability density function (TPDF) based models[21–23] or flamelet based models.[24–29] From this last group of works, Lucchini et al.[26] assessed various assumptions for the flame structure to model a single-hole reacting spray in a constant-volume vessel. Assumptions included well-mixed and flamelet based combustion models. Capabilities of these models were evaluated for low and high-temperature and ambient density conditions in terms of global combustion parameters. From all these group of works it is consistently evidenced that combustion results heavily depend on TCI.

The study of TCI in this work is not limited to the analysis of global combustion parameters and is extended to the description of local phenomena during the ignition sequence and the quasi-steady state of the reacting spray. The work is organized as follows. First, the experimental target Diesel spray setups are described under the "Methodology" section along with the computational setup used to carry-out CFD calculations. The "Inert spray evolution" section comprises the validation of the computational setup for the nonreacting condition. Next, the validation and description of results for the reacting condition are included in the "Reacting spray evolution" section. Finally, concluding remarks are drawn in the "Conclusions" section.

2 Methodology

2.1 Target Diesel spray setup

Target conditions for the present study are based on ECN standards. Fuel injection and thermodynamic conditions studied are summarized in Table 1. Liquid n-dodecane is injected into a quiescent environment through a single-hole nozzle. For the inert condition pure N_2 is present in the ambient. Meanwhile, 15% molar fraction of O_2 is present (in addition to N_2) for the reacting condition. The only varying parameter for this study is the nozzle orifice diameter. Computations are carried-out for ECN Spray A and Spray D which correspond to single-hole nozzles with diameters of 89.4 μm (nozzle reference number 210675) and 190.3 μm (nozzle reference number 209135), respectively.

The results presented in this study are validated using experimental data measured at CMT Motores Térmicos, Sandia National Laboratories or IFP Energies Nouvelles. All measurements are done under the same operating conditions in a constant-pressure vessel (CMT) or in a pre-burn constant-volume vessel (Sandia and IFPEN). The experimental data is available through the ECN.[7]

Table 1. Injection and thermodynamic conditions.

Injection conditions	
Fuel	n-dodecane
Nozzle diameter	89.4 μm – Spray A 190.3 μm – Spray D
Injection pressure	150 MPa
Fuel temperature	363 K
Thermodynamic conditions	
Ambient temperature	900 K
Ambient density	22.8 kg/m^3
Ambient O_2 composition	$X_{O_2} = 0$ – nonreacting condition $X_{O_2} = 0.15$ – reacting condition

2.2 Computational setup

Computations were carried-out using the CFD solver CONVERGE[30] following the traditional Lagrangian-parcel Eulerian-fluid approach. The CFD code uses a cut-cell cartesian method for grid generation. The computational domain is a cylinder with 50 mm radius and 102 mm

length. The base mesh cell size is 2 mm for both Spray A and Spray D cases. A truncated cone-shaped fixed embedding is used near the nozzle region to improve accuracy around this critical zone. The fixed embedding adds 250 μm and 500 μm cells for Spray A and Spray D, respectively. In addition, adaptive mesh refinement (AMR) allows for grid resolution to be added just where is needed based on velocity, temperature and fuel mass fraction gradients. As a consequence, the minimum cell size reached due to AMR is 125 μm for Spray A and 250 μm for Spray D cases.

The Eulerian fluid description is based on the Favre-averaged Navier-Stokes equations solved within a RANS framework. The standard $\kappa - \varepsilon$ model is used with $C_{\varepsilon 1} = 1.55$ to account for round jet correction.[31,32] On the other hand, the liquid-phase is described using the Lagrangian-parcel approach in conjunction with sub-models for droplet breakup, collisions, drag, and evaporation. The Kelvin-Helmholtz (KH) and the Rayleigh-Taylor (RT) models are used for the estimation of droplet breakup. Droplet collisions are accounted for by the no time counter (NTC) model. Droplet drag is predicted with a model that considers variations in the drop shape using a distortion parameter. Lastly, the droplet radius rate of change due to evaporation is estimated based on the Frossling correlation.[33]

The combustion modelling approach is based on detailed chemistry, for which a chemical mechanism with 54 species and 269 reactions[34] has been used. A detailed analysis of this chemical mechanism based on homogeneous reactor calculations can be found in the work by Pérez.[35] In terms of turbulence-chemistry interaction, two approaches have been compared. On the one hand, the well-mixed SAGE detailed chemical kinetics solver[36] (referred to as WM model from this point), which is available in CONVERGE. On the other hand, the unsteady flamelet progress variable (UFPV) model, which has been implemented by the authors. Regarding the WM model, the net production rate of any species k as derived from the chemical mechanism is used to solve the corresponding source term $\dot{\omega}_k$ for governing equations at every cell in the domain, namely mass and energy conservation equations.

As for the UFPV model, it is based on the description of a turbulent flame as a set of strained laminar flamelets.[37] The concept is based on the assumption that the chemical characteristic time is small compared to the physical characteristic time (i.e. a high Damköhler number flow as in the case of Diesel-like combustion applications). In such scenario, turbulence cannot modify instantly and locally the thin layer where combustion is sustained, hence remaining laminar.[38] Flamelets in counterflow configuration are then solved for any species k in mixture fraction (Z) space according to the equation:

$$\frac{\partial Y_k}{\partial t} = \frac{\chi}{2}\frac{\partial^2 Y_k}{\partial Z^2} + \dot{\omega}_k \tag{1}$$

Under this formulation, the chemical source term $\dot{\omega}_k$ is obtained by solving the corresponding reaction rates as defined by the chemical mechanism, meanwhile the strength of convective and diffusive processes is accounted by the scalar dissipation rate (χ), assumed to follow a steady profile[38] defined by:

$$\chi(a, Z) = \frac{a}{\pi} exp\left[-2\left(erfc^{-1}(2Z)\right)^2\right] \tag{2}$$

Equation (2) can then be re-written in such a way that it becomes independent of the strain rate (a) by normalizing the profile using the value of the scalar dissipation rate at stoichiometric conditions (χ_{ST}):

$$\chi(\chi_{st}, Z) = \chi_{st}\frac{F(Z)}{F(Z_{st})} \tag{3}$$

The time evolution of the flamelet is stored as a so-called flamelet manifold parametrized in terms of a progress variable (Y_c), which describes the transition of the mixture from inert to fully burned state as function of a linear combination of species. In this work the progress variable is defined according to:

$$Y_c = 0.75Y_{CO} + Y_{CO_2} + Y_{H_2O} \tag{4}$$

At this point, the manifold generated by solving the PDE system is laminar. TCI is then accounted using a presumed Probability Density Function (PDFs) approach for the mixture fraction and the scalar dissipation rate assuming statistical independence between these two variables.[39] For the first of these variables a beta function defined by the mean value of Z ($\tilde{Z}$) and its variance ($\widetilde{Z''^2}$) yielding to $P_Z\left(Z; \tilde{Z}, S\right)$, where S is the so-called segregation factor calculated as $S = \widetilde{Z''^2}/\left(\tilde{Z}(1-\tilde{Z})\right)$. As for the scalar dissipation rate, a log-normal function with $\sigma = \sqrt{2}$ is used[40] fielding to $P_\chi(\chi_{st}; \widetilde{\chi_{st}}, \sigma)$. Once PDFs have been defined as functions of the independent variables Z and χ_{st}, any average value ($\tilde{\psi}$) in the manifold is defined by:

$$\tilde{\psi}\left(\tilde{Z}, S, \widetilde{\chi_{st}}, \tilde{t}\right) = \int_0^\infty \int_0^Z \psi(Z, \chi_{st}, \tilde{t}) P_Z\left(Z; \tilde{Z}, S\right) P_\chi(\chi_{st}; \widetilde{\chi_{st}}, \sigma)\, dZ\, d\chi_{st} \tag{5}$$

Considering the re-parametrization of the laminar solution in terms of the progress variable, the average values in the manifold can be expressed as $\tilde{\psi} = \tilde{\psi}\left(\tilde{Z}, S, \widetilde{\chi_{st}}, \widetilde{Y_c}\right)$. This re-parametrization is possible under the assumption that $\widetilde{Y_c}$ increases monotonically such that there is a bijective relationship with $\tilde{t}$.[40] Equation (6) is then used for the integration of χ (where J only depends on $\tilde{Z}$ and S) and relates $\tilde{\chi}$, recovered from the CFD calculation according to Equation (7), and $\widetilde{\chi_{st}}$ used to query the manifold.

$$\tilde{\chi} = \left(\int_0^{\infty} \chi_{st} P_{\chi}(\chi_{st}; \widetilde{\chi_{st}}, \sigma) d\chi_{st}\right)\left(\frac{1}{F(Z_{st})}\int_0^{Z} F(Z) P_Z\left(Z; \tilde{Z}, S\right) dZ\right) = \widetilde{\chi_{st}} J\left(\tilde{Z}, S\right) \tag{6}$$

$$\tilde{\chi} = C_{\chi} \frac{\varepsilon}{\kappa} \widetilde{Z''^2} \tag{7}$$

It is worth mentioning that the manifold is constructed independently from the CFD calculation by creating lookup tables where mean species mass fractions and the mean progress variable source term can be queried as $\tilde{Y}_k^{tab}\left(\tilde{Z}, S, \widetilde{\chi_{st}}, \widetilde{Y_c}\right)$ and $\widetilde{\dot{\omega}Y_c}^{tab}\left(\tilde{Z}, S, \widetilde{\chi_{st}}, \widetilde{Y_c}\right)$, respectively. The lookup tables are discretized with 41 points for $\tilde{Z}$, 17 points for S, 27 points for $\widetilde{\chi_{st}}$ and 51 points for $\widetilde{Y_c}$.

Coupling of the UFPV model within the CFD framework is achieved through the chemical source term of the species transport equation ($\dot{\omega}_k$), which is calculated as:

$$\tilde{\dot{\omega}}_k = \frac{\tilde{Y}_k^{tab}\left(\tilde{Z}, S, \widetilde{\chi_{st}}, \tilde{Y}_c(t + \Delta t)\right) - \tilde{Y}_k^{cell}(t)}{\Delta t} \tag{8}$$

In Equation (8), Δt is the CFD time-step, $\tilde{Y}_k^{cell}$ is the species mass fraction at the cell and $\tilde{Y}_k^{tab}$ is the species mass fraction tabulated in the manifold in the subsequent timestep, defined in terms of $\tilde{Y}_c(t + \Delta t)$, which is calculated as:

$$\tilde{Y}_c(t + \Delta t) = \tilde{Y}_c(t) + \widetilde{\dot{\omega}Y_c}\left(\tilde{Z}, S, \widetilde{\chi_{st}}, \tilde{Y}_c(t)\right)\Delta t \tag{9}$$

To advance in the manifold using Equation (9), $\tilde{Y}_c(t)$ is calculated following the definition in Equation (4) and $\widetilde{\dot{\omega}Y_c}$ (generic nomenclature for $\partial\tilde{Y}_c/\partial t$) is retrieved from the manifold. $\tilde{\dot{\omega}}_k$ is then used in the transport of species.

Finally, there's an additional aspect of the UFPV model formulation worth mentioning. In this work a variant named UFPV-0 is introduced. For this variant, the manifold is constructed following the same structure as for the UFPV case, but no presumed-PDF integration is taking into account, i.e. this should correspond to a tabulated laminar flamelet model. This variant seeks to facilitate the analysis of differences induced by the sub-grid flame structure formulation, namely the well-mixed and the flamelet-like structure.

3 Inert spray evolution

3.1 Validation of the computational setup

The validation of the computational setup is carried-out by comparing global and local quantities with experimental data available within the ECN. Following ECN guidelines, spray tip penetration is defined as the axial distance to the furthest location where the mixture fraction Z reaches a value of 0.001. Figure 1 shows the experimental spray tip penetration value plotted with a solid black line with a gray shadow around the 95% confidence interval and CFD predictions for Spray A and Spray D (spray tip penetration and liquid length). The same computational setup and model settings have been used for both nozzles. An excellent agreement is observed for Spray A tip penetration, while a slight underprediction is observed for the larger nozzle. Given the fact that no change has been made in the modelling setup for both nozzles the agreement is satisfactory.

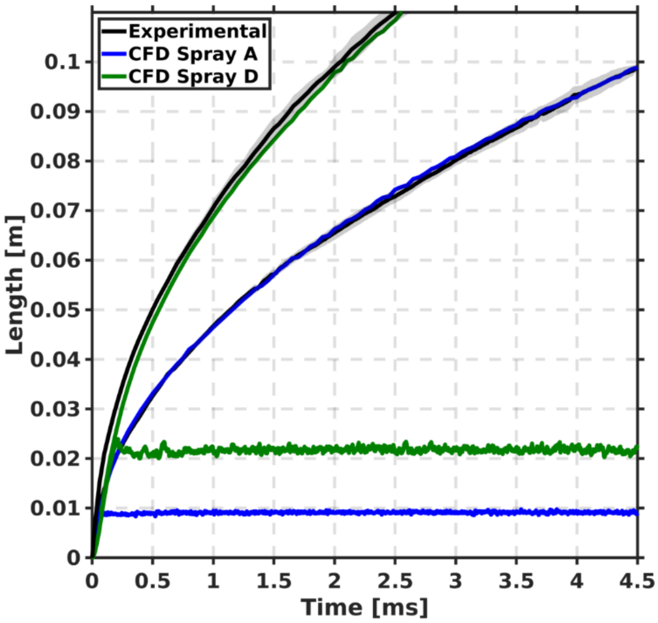

Figure 1. Spray tip penetration and liquid length for inert Spray A and Spray D.

In terms of local quantities, the computational setup is validated for Spray A (no experimental data available for Spray D). Mixture fraction Z and its root mean square (Z_{rms}) and axial velocity fields are validated by comparing axial and radial profiles. Radial and axial coordinates have been normalized by the equivalent diameter (d_{eq}) of each nozzle i.e. $r^* = r/d_{eq}$ and $x^* = x/d_{eq}$. The equivalent diameter is defined as a function of the nozzle effective diameter (d_0) and the ratio of fuel density (ρ_f) and air density (ρ_a) and is calculated as $d_{eq} = d_0\sqrt{\rho_f/\rho_a}$. Different nozzles have been used for experimental and CFD work. As previously mentioned, nozzle 210675 (same nozzle used for the experimental measurement of spray tip penetration, ignition delay and lift-off length) has been modeled for the Spray A case. Meanwhile, nozzle 210677 has been used for the experimental work to measure Z and nozzle 210678 has been used to measure axial velocity. Nominal diameters for the three nozzles are 89.4 μm, 83.7 μm and 88.6 μm for the 2010675, 210677 and 210678 reference numbers, respectively. Normalization of spatial coordinates allows for a better comparison of experimental and CFD results. Figure 2 and Figure 3 show axial and radial profiles for the above-mentioned local quantities. From the left-hand panel in Figure 2 the computational setup is seen to be successful in predicting Z (solid line) and Z_{rms} (dotted line) within the limit of the 95% confidence interval of the experimental observation along the spray axis. These two variables are inputs for the UFPV combustion model. Similarly, the right-hand panel in Figure 2 also shows good agreement with experimental data in terms of axial velocity. Differences for x* < 60 are expected due to the measurement uncertainty in that region corresponding to the limit of the laser sheet used in the PIV experiments.[10]

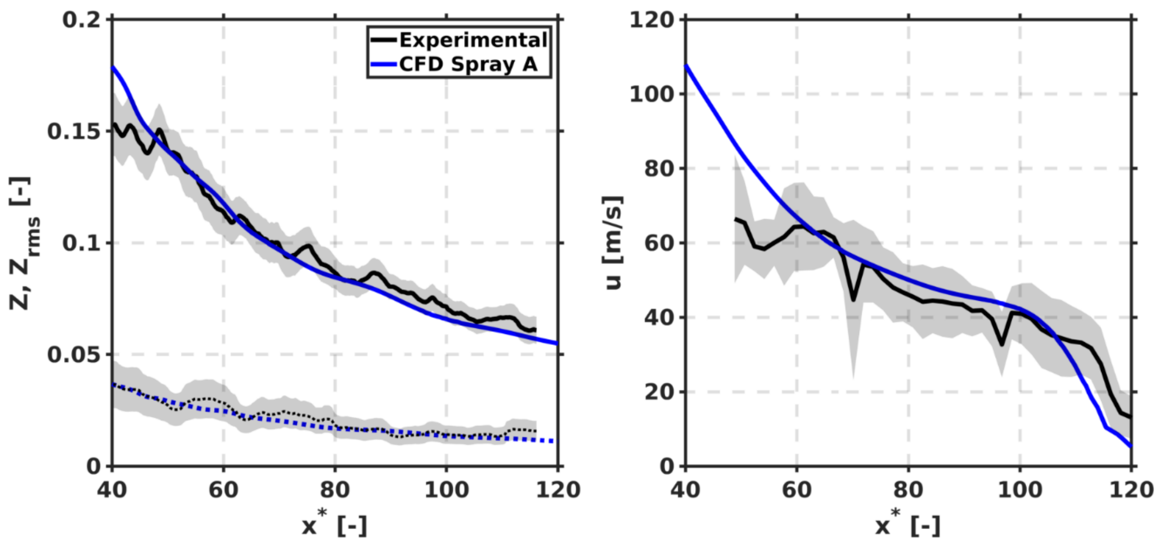

Figure 2. Inert Spray A axial profiles for mixture fraction (solid line) and mixture fraction rms (dotted lines) at 5 ms and axial velocity at 1.5 ms.

Further validation is shown in terms of radial profiles for Z and Z_{rms} at two axial locations in Figure 3 and Figure 4. At 50 d_{eq} the profiles predicted by CFD for both variables (left-hand panel) agree well with the experimental observations. As expected from the axial profiles, at 90 d_{eq} both Z and Z_{rms} CFD results show slightly narrower profiles although in general terms the predictions still agree well with experiments.

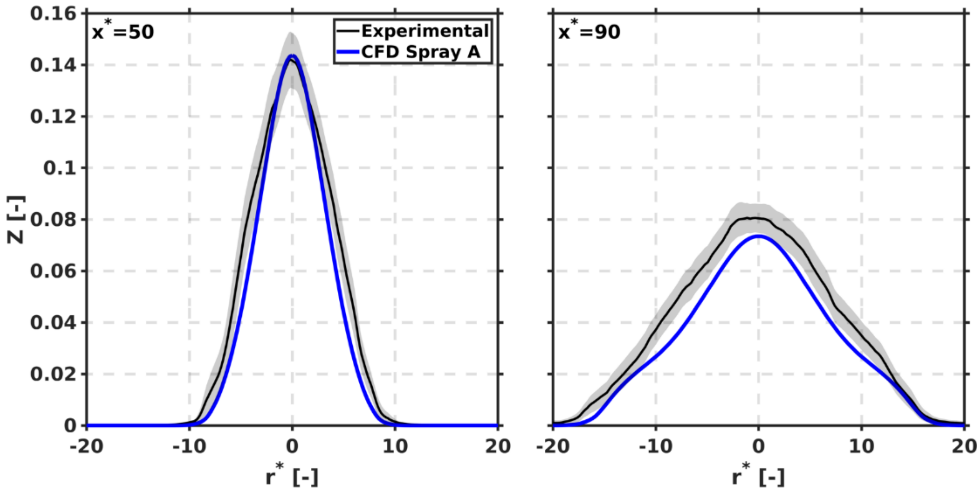

Figure 3. Mixture fraction radial profiles for inert Spray A at 5 ms.

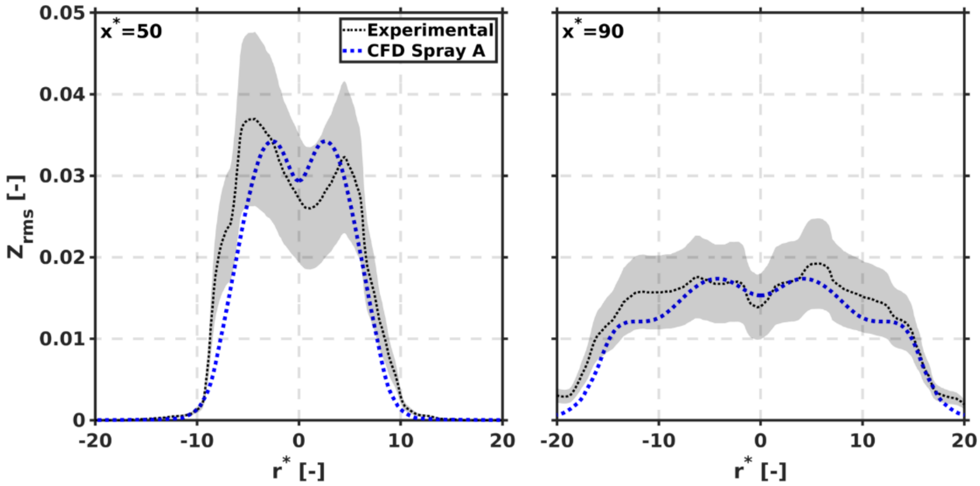

Figure 4. Mixture fraction rms radial profiles for inert Spray A at 5 ms.

3.2 Local residence time

To provide an additional local indicator of mixing intensity, a local residence time has been defined based on mixing trajectories (Appendix A. Mixing trajectories) as the time spent per unit of equivalence ratio (ϕ) according to:

$$\frac{dt^*}{d\phi} = -\frac{dt^*}{dl}\frac{dl}{d\phi} = -\left(\sqrt{\left(u + u_{dif}\right)^2 + \left(v + v_{dif}\right)^2}\right)^{-1}\frac{dl}{d\phi} \tag{10}$$

The physical meaning of this parameter is the time needed to change a unit value of equivalence ratio along a mixing trajectory or, in other words, the time spent at a given ϕ value. This parameter is made up of the product of two terms. First, the rate of residence time per length unit (dt^*/dl) is solved considering convective and diffusive contributions (Equation (12) and Equation (13)). Second, $dl/d\phi$ is obtained from the spatial gradient of ϕ as projected along the direction defined by the velocity field (i.e. a mixing trajectory). To the best of the authors' knowledge, this is the first time that an attempt has been made to analyze the mixing process in terms of local residence time for spray applications.

Figure 5 shows local residence time for both Spray A and Spray D under inert conditions. The definition of the residence time in terms of the change of equivalence ratio enables a direct comparison between both nozzle orifices. The analysis of local residence time is then made at $4\ ms$, time at which the spray is already at quasi-steady state. A sample of mixing trajectories (solid lines) and the iso-contour for $\phi = 1$ (dashed line) are also shown. For visualization purposes the color map is adjusted to logarithmic scale. It can be observed how the structure is similar for both sprays with increasing values of residence time along any trajectory when moving downstream from the orifice. Among trajectories at the same axial normalized coordinate (consequently at a similar equivalence ratio) there is also an increase of $dt^*/d\phi$ with a local maximum near the spray radius. In summary, residence time grows when moving away from the orifice, both in axial and radial direction.

Due to the fact that the mixture fraction (hence equivalence ratio) is a conservative scalar, one can state that the convective plus diffusive flow of this variable remains constant between two mixing trajectories and develops with an almost constant angle compared to the axis. By integrating both the mixing trajectories and the residence time concepts, the mixing field created by the spray can be viewed as a set of mixers starting close to the nozzle, which then move away from it entraining air and spending more time on a given equivalence ratio, as farther locations are reached.

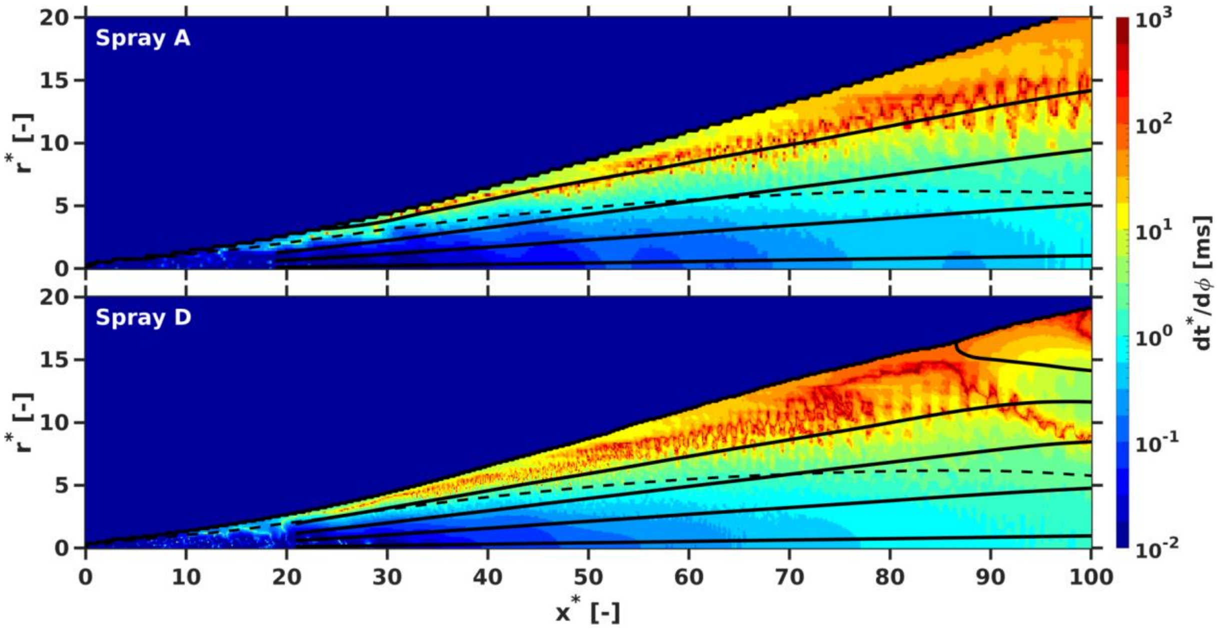

Figure 5. Local residence time for inert Spray A (top) and Spray D (bottom). Spatial coordinates have been normalized by d_{eq}.

To enable further comparison between both nozzles, the upper part of Figure 6 shows spray radius with a solid line and iso-contours of $\phi = 1$ (dashed line) and $\phi = 2$ (dotted line). It is then confirmed that the normalization of spatial coordinates of the two different nozzles by d_{eq} results in the same value of ϕ for a given value of (x^*, r^*). Additionally, if $dt^*/d\phi$ is studied along the reference iso-contours of ϕ (bottom part of the figure) it is then verified that this parameter increases with axial distance, in agreement to the contours shown in Figure 5. Furthermore, for the same value of ϕ, Spray A is characterized by shorter local residence time (thus faster mixing) compared to Spray D. Going back to the previous description of the spray as a set of mixers defined by the mixing trajectories and leaning out while moving away from the nozzle, the time spent on a given equivalence ratio will be always longer for the larger nozzle by a factor around 2, i.e. approximately equal to the nozzle orifice increase. This has an effect on combustion development, as the following sections will prove.

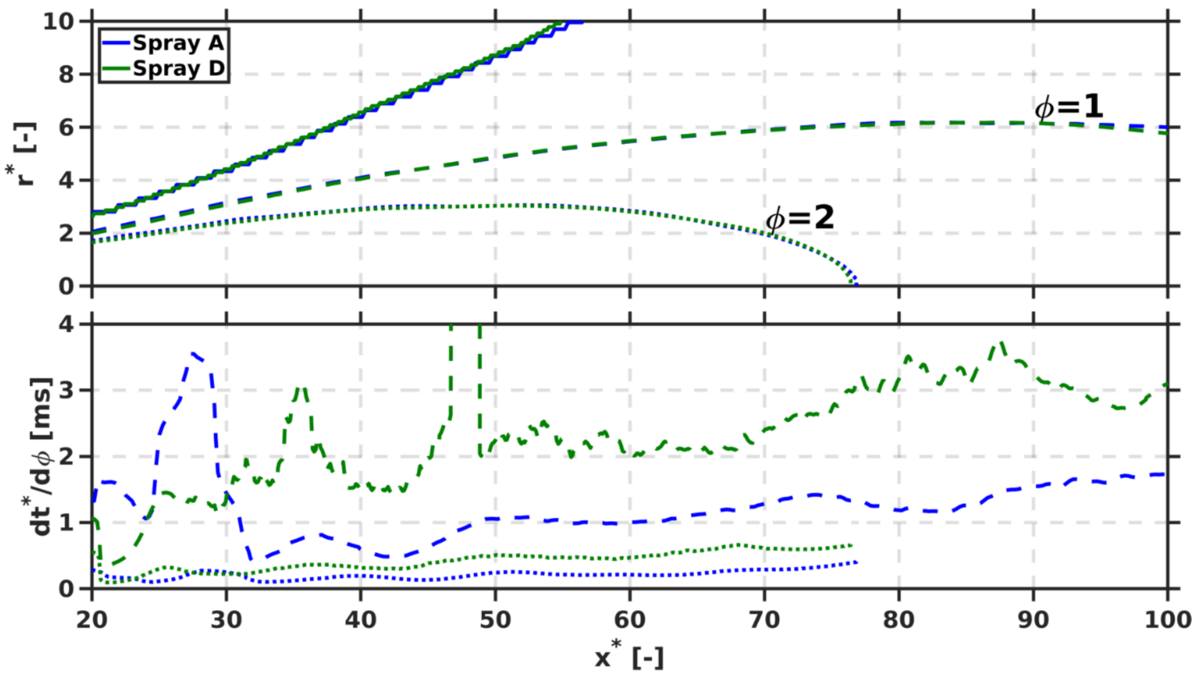

Figure 6. Top: Spray radius R, and iso-contours of $\phi = 1$ (dashed line) and $\phi = 2$ (dotted line) for Spray A and Spray D. Bottom: Corresponding local residence time along iso-contours of $\phi = 1$ and $\phi = 2$. Profiles of $dt^{*}/d\phi$ have been smoothed with a moving average algorithm. Spatial coordinates have been normalized by d_{eq}.

To conclude the description of the inert spray evolution, Figure 7 shows the scalar dissipation rate at stoichiometric conditions and mixture fraction rms for Spray A and Spray D, which are input parameters for flamelet models such as the UFPV model. These variables are plotted along the same reference iso-contours of ϕ shown in the top panel of Figure 6. Results show that higher χ_{ST} is predicted for Spray A for a given ϕ, in line with faster mixing occurring for the smaller nozzle, which creates more important gradients. On the contrary, there are virtually no differences among the nozzles in terms of mixture fraction rms. The implications of these last observations will be further discussed in the description of the reactive spray in the next sections.

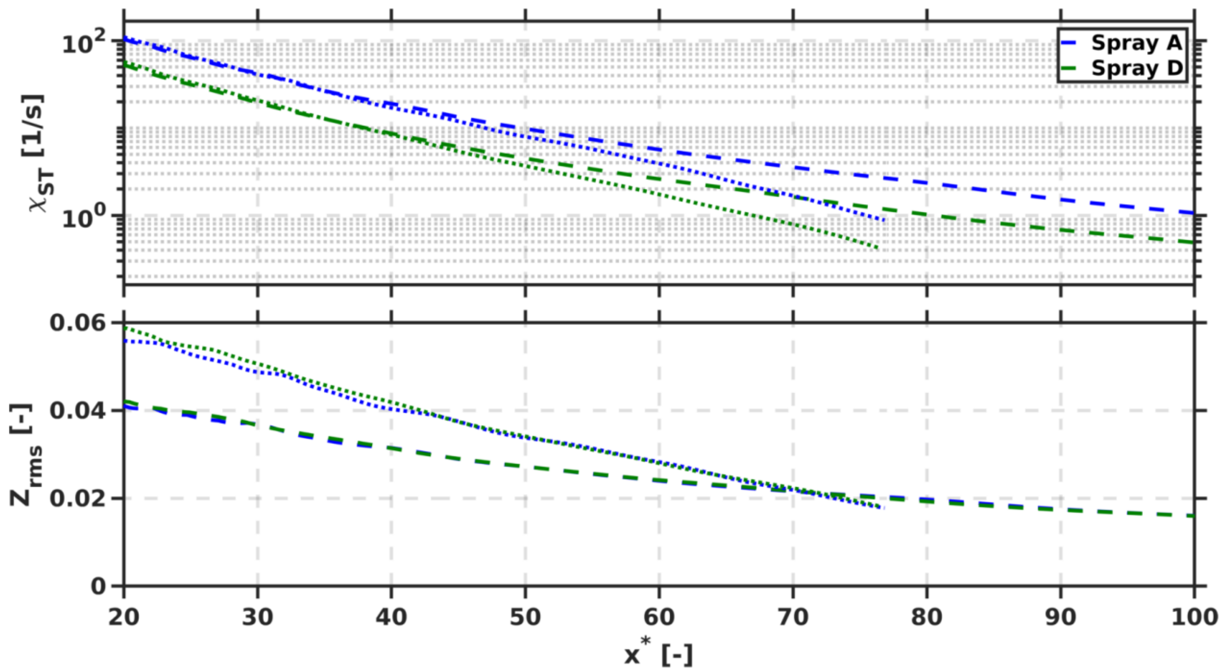

Figure 7. Scalar dissipation rate at stoichiometric conditions and mixture fraction rms along iso-contours of $\phi = 1$ (dashed line) and $\phi = 2$ (dotted line) for Spray A and Spray D.

4 Reacting spray evolution

4.1 Validation of the computational setup

The computational setup validated for inert conditions is used to simulate reacting Spray A and Spray D according to the conditions summarized in Table 1. Both the WM model and the flamelet-based UFPV model are used. Figure 8 compares results for spray tip penetration. As in the validation for the inert setup, here the spray tip penetration is defined as the axial distance from the nozzle where Z reaches a value of 0.001. The experimental result is plotted with a black solid line with gray shadow to indicate measurement uncertainty. Excellent agreement between CFD and experimental results is observed for Spray A, meanwhile for Spray D a slight over-prediction is observed for both combustion modelling approaches, while the agreement is better for UFPV. Differences between both predictions are linked to the differences in ignition delay, which triggers an acceleration of the flow.[41] In addition to spray tip penetration, the setup is also validated for axial velocity with available PIV measurements for Spray A.[10] Figure 9 compares results for this variable along the spray axis. It is shown that both models predict similar results which match well the experimental data.

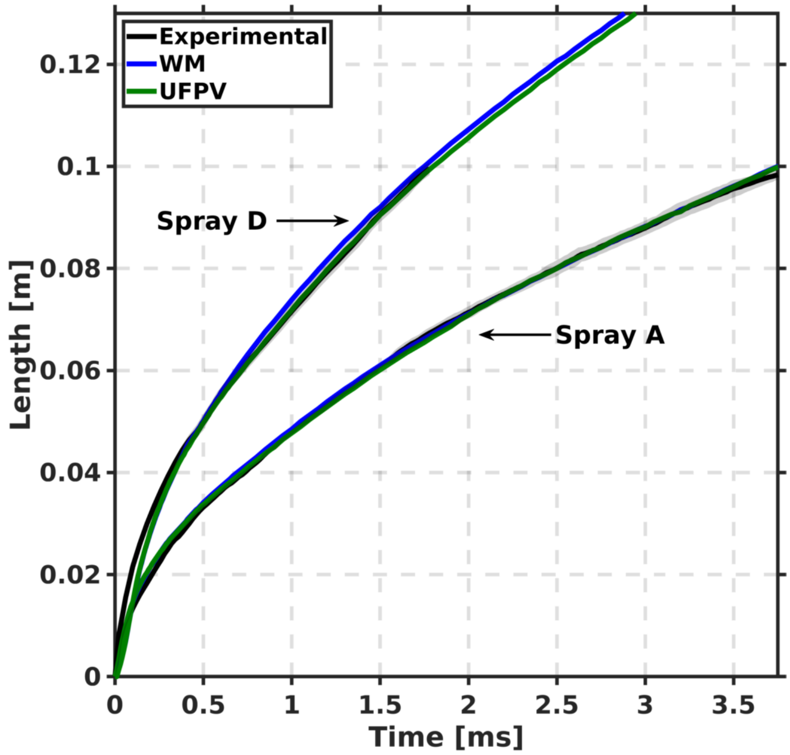

Figure 8. Spray tip penetration for reacting Spray A and Spray D.

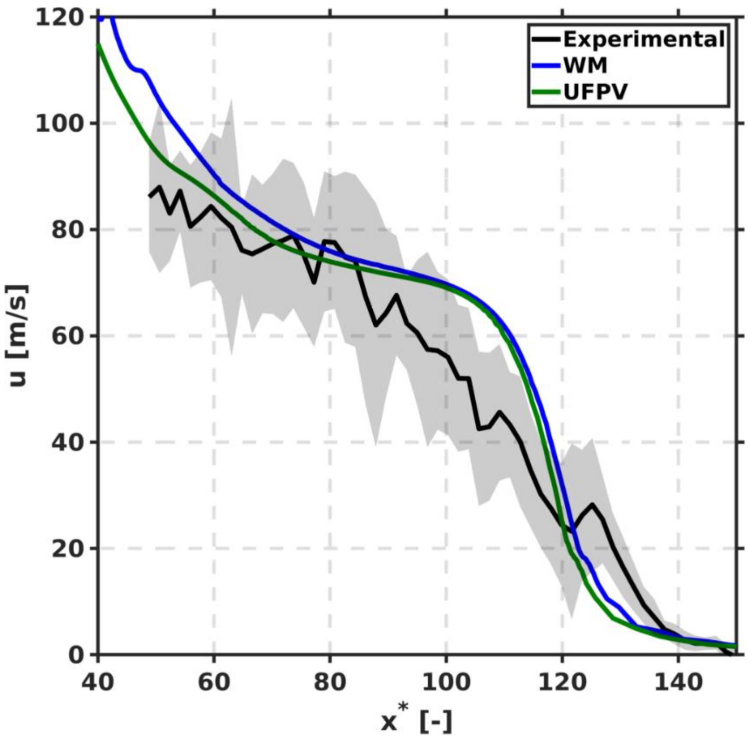

Figure 9. Axial velocity along spray axis for reacting Spray A at 1.5 ms.

After the validation of the reacting flow evolution, global combustion parameters are analyzed here. Hence, CFD results for ID and LOL are quantitatively compared to experiments. On the experimental side, ID and LOL are the result of analyzing schlieren and OH* chemiluminescence images, respectively. On the CFD side, ID and LOL are obtained following ECN guidelines. ID is defined as the time from start of injection at which dT_{max}/dt is maximum, with T_{max} being the maximum temperature in the domain. For LOL, the definition is based on OH mass fraction. At each time after the start of combustion LOL is marked at the closest position to the nozzle to reach 14% of the maximum OH mass fraction. Then, an average value is obtained once LOL has stabilized.

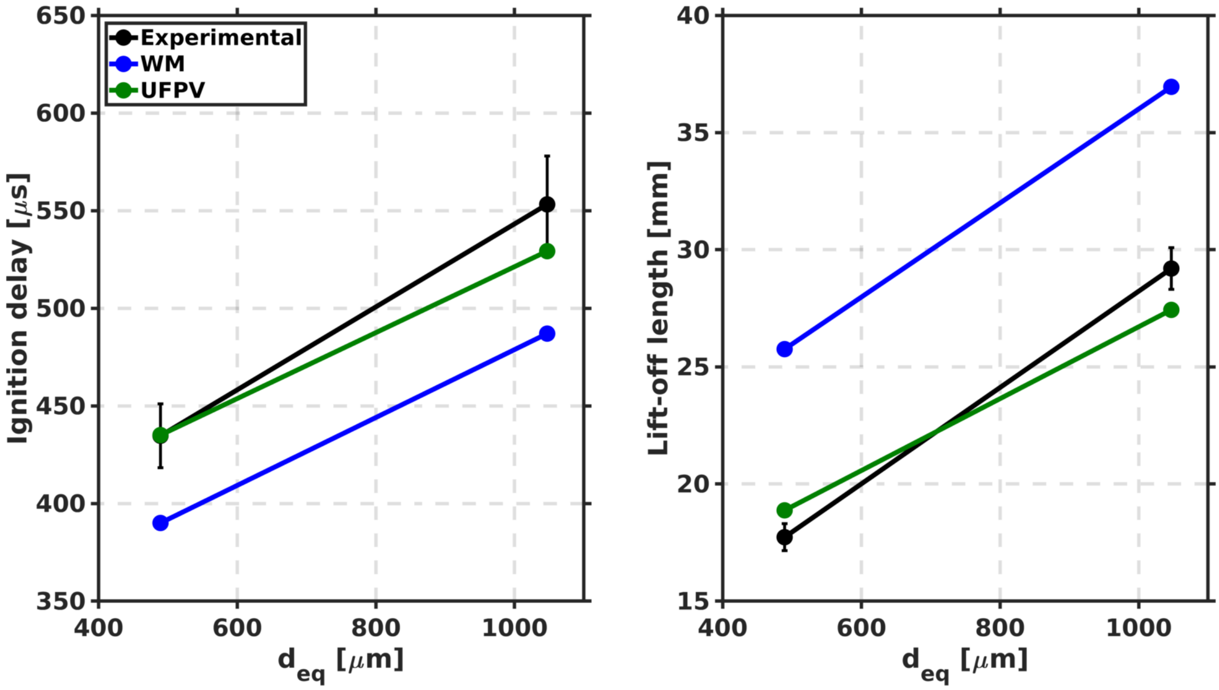

Figure 10. Ignition delay and lift-off length for Spray A and Spray D.

Figure 10 shows differences in predicted values compared to experimental results represented with black dots (vertical lines on top mark the standard deviation of the measurement). A slight underprediction of ID and an overestimation of LOL is observed when the WM model is used for both nozzles. Differences decrease with the use of the UFPV model. In this case, ID matches well with the experiment for Spray A with a slight underprediction for Spray D. As for LOL maximum deviation from the experimental values is less than 7%. The detailed analysis of both quantitative parameters will be related to the autoignition sequence and steady flame structure in the following sections, so that observed differences among nozzles can be understood.

4.2 Spray A auto-ignition sequence

In this section, a detailed analysis of the ignition sequence of Spray A is made comparing results from the WM model and the UFPV model. The analysis makes use of the mixing trajectories concept, which enables bridging a link between combustion development in the physical space and in the equivalence ratio-temperature ($\phi - T$) maps.

First, the auto-ignition sequence predicted using the WM model is presented in Figure 11. The contour of the local heat release rate (HRR) is plotted along with the spray radius. A dashed green line is plotted at the location of the iso-contour of the most reactive equivalence ratio (ϕ_{MR}). This parameter indicates the mixture composition showing the fastest ignition process when considering homogeneous reactors (HR) calculations starting from the inert adiabatic mixing condition. The HR 0D calculations done for this particular case and chemical mechanism show that the shortest ID corresponds to $\phi_{MR} = 1.32$ and is in line with findings already published in the literature.[42] The last panel of the figure shows the spatially integrated HRR with black dot markers to highlight the time instants at which the local HRR was depicted.

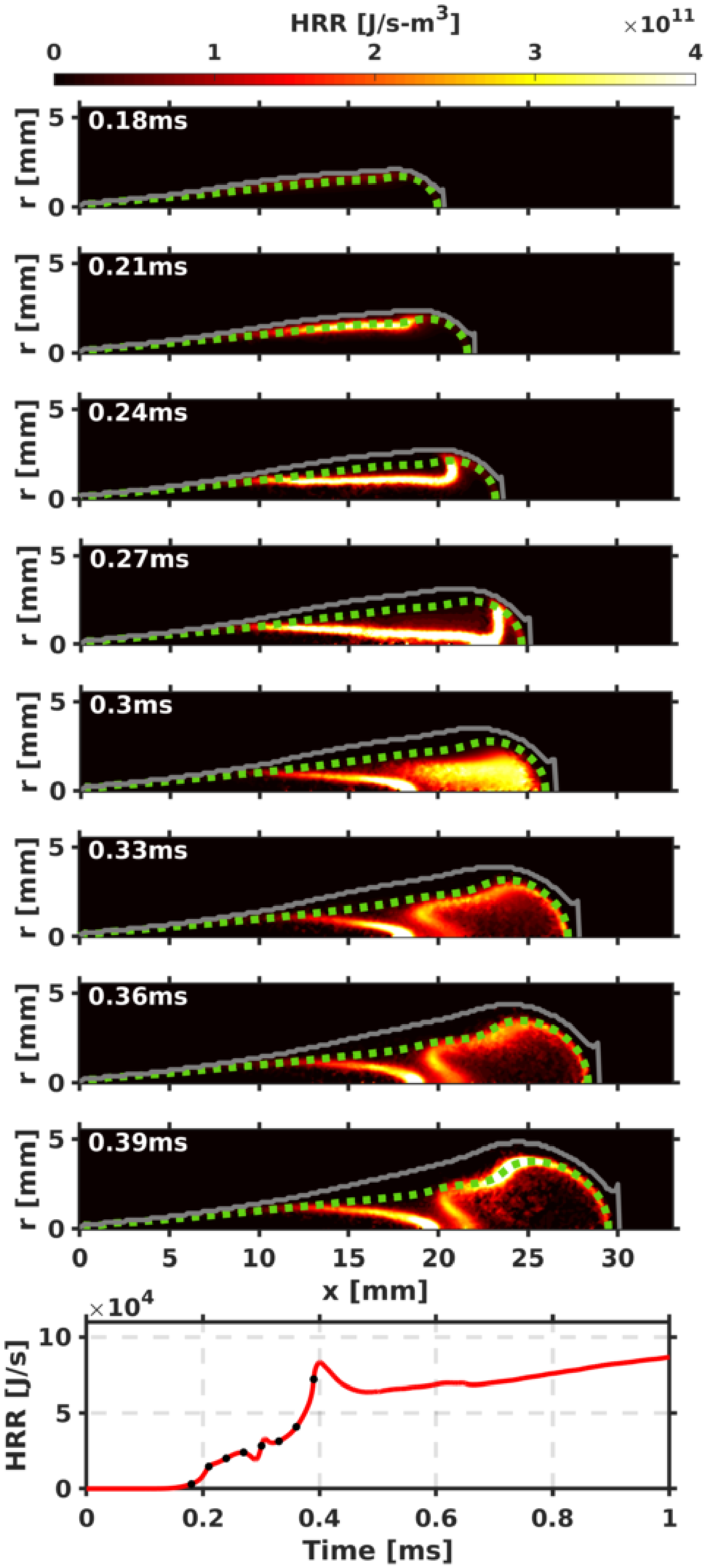

Figure 11. Time and spatially resolved local HRR for Spray A using the WM model. Dashed green line drawn at ϕ_{MR}. Bottom plot shows the integrated HRR, where markers indicate the timings of the local HRR contours.

The sequence depicted in Figure 11 shows how the first-stage of ignition starts taking place at around 0.21 ms near the spray radial periphery and locations close to ϕ_{MR}. This observation agrees well with the idea that ignition requires a certain degree of mixing of the injected fuel to reach reactive enough equivalence ratios and temperature conditions, as well as some residence time for chemistry to progress. The location of this low-temperature heat release near the spray border is consistent with longer residence time at the spray radial periphery, as described in the "Local residence time" section. Starting at 0.21 ms some sort of low-temperature heat release wave starts progressing towards richer mixtures (with a consistent increase in the integrated HRR in the last panel of the figure) in the spray core followed by a quasi-homogeneous state of heat release at 0.3 ms. Next, an abrupt decrease in heat release throughout the spray cross section is observed between 0.33 ms to 0.36 ms to then make way to the second-stage ignition occurring around the most reactive equivalence ratio iso-surface. The penultimate row in the panel shows the situation at the ID timing based on dT_{max}/dt, which occurs at 0.39 ms, with the start of an intense heat release zone around the most reactive equivalence ratio location. After this point, a diffusion flame is established and the integrated HRR is controlled by mixing as seen in the last row of the figure.

The onset time for the appearance of low-temperature heat release at around 0.21 ms, the consequent propagation towards the spray core followed by a quasi-homogeneous state of heat release and finally the decrease in chemical activity prior to the second-stage ignition are all features that are in line with experimental observations and supporting modelling results presented in the work by Dahms et al.[11] At the time of the second-stage ignition (penultimate panel in Figure 11) there are two distinctive heat release zones in the spray: a first cone-shaped structure associated with low-temperature heat release that was already present at 0.3 ms, and a high-temperature heat release zone near the spray radial periphery along the ϕ_{MR} contour. It should also be emphasized that this high-temperature heat release zone confined around ϕ_{MR} is in disagreement with the above-mentioned experimental observations (supported by modelling results)[11] where main ignition takes place over a wide range of equivalence ratios.

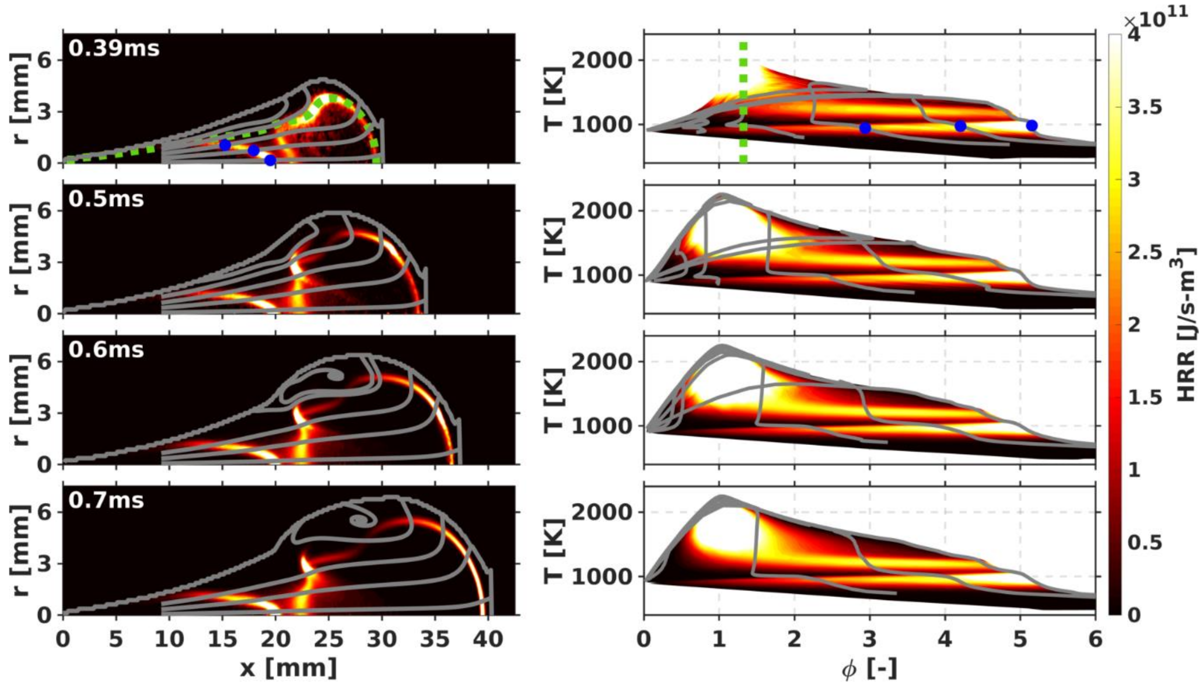

Figure 12. Time resolved local HRR in spatial coordinates (panels on the left) and in $\phi - T$ coordinates (panels on the right) for Spray A using the WM model. Dashed green line drawn at ϕ_{MR}. Blue markers to highlight the low-temperature heat release zone.

Finally, to analyze the post-ignition sequence Figure 12 shows on the left panels HRR contours in spatial coordinates and on the right panels HRR contours plotted in $\phi - T$ coordinates. Mixing trajectories are included in both representations, with the purpose of linking spatial and $\phi - T$ coordinates. At ID timing (top part of Figure 12) two distinctive characteristics mentioned in the analysis of the auto-ignition sequence can be confirmed. On the one hand, the occurrence of second ignition at ϕ_{MR} is clearly observed on the $\phi - T$ map. The intense HRR spot observed in spatial coordinates near the spray radial periphery corresponds to the highest temperature in the $\phi - T$ map, which at ID time takes place at the vertical dashed line drawn at ϕ_{MR}. On the other hand, low-temperature heat release is observed to occur over a wide equivalence ratios range, when represented in $\phi - T$ coordinates. The farthest point from the nozzle at around $x \cong 20\ mm$ on the first mixing trajectory (closest to the spray axis) corresponds to the point at $\phi \cong 5$, the next two points at $\phi \cong 4$ and $\phi \cong 3$ correspond to blue round markers on the second and third mixing trajectories, respectively. Furthermore, for all three trajectories a second low intensity heat release front occurs just downstream of the initial one at a slightly higher temperature (around $1200\ K$). This zone will later result in the LOL stabilization region. Both low and medium temperature heat release regions remain essentially steady for the remaining part of the reacting spray evolution, as they are located in the quasi-steady part of the spray.

A noticeable feature of the autoignition sequence for the WM model is that, beyond 0.39 ms, the high-temperature heat release spot observed in spatial coordinates splits into two fronts. One of the fronts progresses in upstream direction, towards the position at which LOL will later stabilized. The other front moves downstream towards the spray head. The progress of this second heat release front in spatial coordinates can be linked to $\phi - T$ space through the mixing trajectories, starting from the axis towards higher radial coordinates in the physical space, which corresponds to lines from richer to leaner values in the $\phi - T$ space. At 0.5 ms the heat release front has not yet reached the two trajectories closest to the axis. Consequently, on the $\phi - T$ map these two mixing trajectories have still not reached the maximum temperature on the map (evidenced by the almost horizontal temperature between $\phi \cong 2$ and $\phi \cong 3$). At 0.6 ms the heat release front has just passed through the second mixing trajectory closest to the axis, causing it to reach the maximum temperature on the $\phi - T$ map for any equivalence ratio value. Lastly, at 0.7 ms the heat release front has reached the spray axis and all mixing trajectories have reached the maximum temperature for any equivalence ratio value.

In an attempt to establish an intermediate situation that enables a better understanding of the changes when moving from WM results to UFPV results, Figure 13 shows the auto-ignition sequence for the modified version of the UFPV model, denoted as UFPV-0, where the flamelet manifold has been built without any PDFs integration (neither for mixture fraction nor for scalar dissipation rate) to be able to capture spatial details that otherwise are softened by the presumed-PDF integration as later seen in Figure 14. In this way, WM to UFPV-0 (Figure 12 vs Figure 13), shows the effect of changing the sub-grid description of the flame structure (from a WM to a flamelet formulation) while UFPV-0 to UFPV (Figure 13 vs Figure 14), evaluates the influence of TCI by means of presumed-PDF integration.

Figure 13 shows initial heat release occurring from the spray radial periphery towards the spray axis before reaching a stabilized cone-shaped low-temperature heat release front at 0.34 ms. The evolution is more volumetric than for the WM model, where a well-defined low-temperature reaction front was observed in the initial stages (0.24 ms). Furthermore, reactions tend to be located further downstream compared to WM results already from the start, probably due to the inhibiting effect of scalar dissipation rate in locations close to the nozzle (Figure 7). The quasi-homogeneous heat release state already observed for the WM model at 0.3 ms seems to be occurring also for UPFV-0 at 0.38 ms, although spatially limited to a region closer to the spray tip and near the spray axis. After that, heat release decreases within this reaction zone, which slightly recedes upstream and towards the spray radial periphery. Then, high-temperature ignition takes place (last contour plot in Figure 13). In agreement with the whole spray ignition sequence, the high-temperature heat release starts at around 27 mm, further downstream than for WM results (slightly upstream of 25 mm).

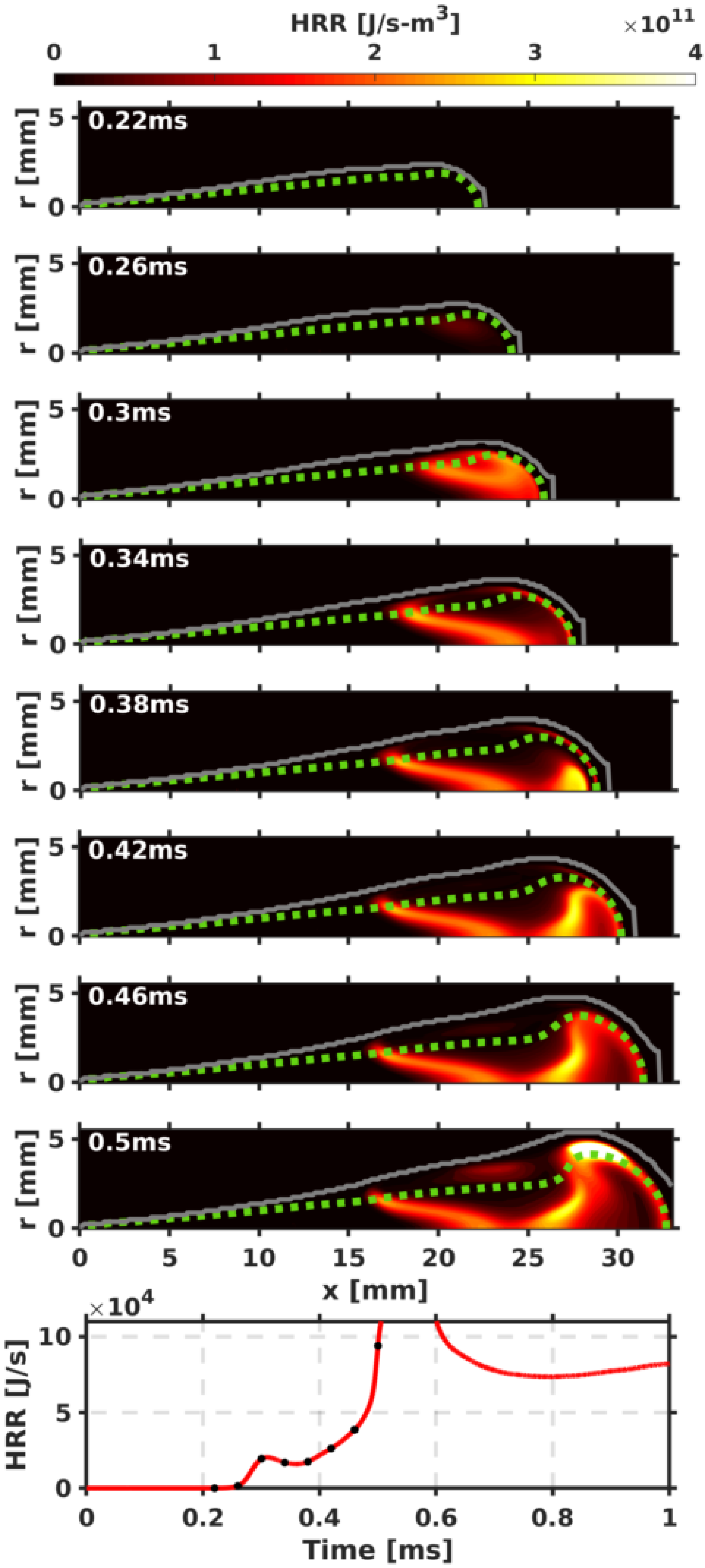

Figure 13. Time and spatially resolved local HRR for Spray A using the UFPV-0 model. Dashed green line drawn at ϕ_{MR}. Bottom plot shows the integrated HRR, where markers indicate the timings of the local HRR contours.

The same image layout used to depict the auto-ignition sequence for WM model results has been used for UFPV model results. Consequently, Figure 14 shows HRR contours accompanied by the spray radius and the ϕ_{MR} iso-contour (green dashed line). Several time instants are included up until ID time at 0.44 ms (penultimate row in Figure 14). Aside from the differences in timing, some features in ignition will be discussed to evidence the differences in ignition description.

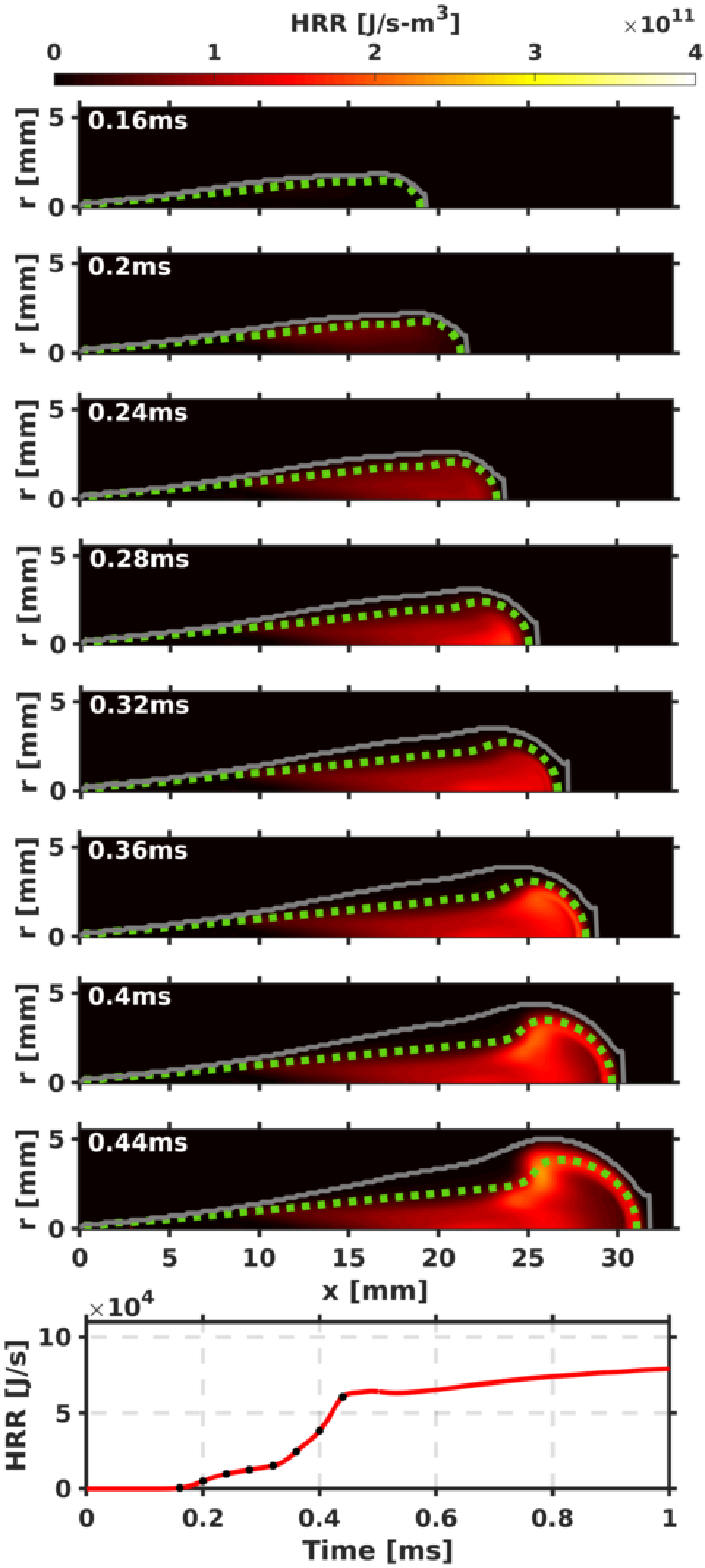

Figure 14. Time and spatially resolved local HRR for Spray A using the UFPV model. Dashed green line drawn at ϕ_{MR}. Bottom plot shows the integrated HRR, where markers indicate the timings of the local HRR contours.

In a similar way as observed in WM model results, first-stage ignition starts taking place near the spray radial periphery. Nonetheless, unlike predictions using the WM model, the UFPV model predicts this first-stage ignition as taking place in a much broader area in the spray and not only around the most reactive equivalence ratio as derived from HR results. Keeping in mind that the color scale is the same, the intensity of this initial ignition is lower for the UFPV model (as also seen in the integrated HRR plot at the bottom of the figure), which will be a constant feature through the whole ignition sequence. Next, heat release progresses towards the spray core with richer mixtures and reaches a quasi-homogeneous reaction state at around 0.32 ms close to the spray head, comparable to WM model results at 0.3 ms. However, the low-temperature heat release front is not confined to a concrete region in the spray as it was predicted in the latter model. Additionally, not such an abrupt decrease in chemical activity throughout the spray cross section prior to second-stage ignition is observed with the UFPV model (0.36 to 0.4 ms) as was the case for WM (0.33 ms). At 0.4 ms an increase in HRR level is visible near the spray radial periphery close to the spray tip, where second-stage ignition eventually takes place at 0.44 ms. This observation is consistent with high residence time and low χ_{ST}, both favorable for auto-ignition.[43] Compared to WM results, where the main ignition was observed slightly upstream of 25 mm (penultimate panel on Figure 11), UFPV tends to produce a main ignition site slightly downstream of 25 mm. As in the WM case, the ID time coming from the analysis of dT_{max}/dt matches the timing of high-temperature HRR (last row of Figure 14)

Observed differences between WM and UFPV results obey to two factors. First, UFPV makes use of reaction source terms based upon the flamelet formulation, compared to the homogeneous reactors in the WM model. Second, UFPV uses a presumed-PDF approach to account for turbulent fluctuations, which are neglected in the WM model. Regarding differences between UFPV-0 and UFPV (Figure 13 vs Figure 14), the effect of presumed-PDF becomes quite apparent. The main effect is the smoothing of gradients that results in a more volumetric description of the ignition event of the spray. A second important feature is the decrease in heat release seen both in the spray HRR contours and in the integrated HRR plot. Finally, while the spatial location of all such events is pretty similar, the timing becomes slightly advanced for UFPV. All these results are a consequence of the averaging of the different igniting flamelets.

Based on the conceptual descriptions and experimental observations reported in the literature[11] the UFPV model successfully captures auto-ignition key features of ECN Spray A. Low-temperature reactions are seen to be starting at the spray radial periphery and then move towards the spray axis. The quasi-homogeneous state of low-temperature heat release and the subsequent decrease in chemical reactivity before the main ignition event are also captured by the model. Finally, the model predicts second-stage ignition as taking place in a broader range of mixtures and not being confined around ϕ_{MR}. Diffusion phenomena induced by the scalar dissipation rate as well as the presumed-PDF approach allows the UFPV model to capture this last feature that is not reproduced in a well-mixed approach. Finally, the inclusion of such sub-grid diffusion effects by means of χ_{ST} delays the overall temporal sequence of auto-ignition in around 0.1 ms compared to the well-mixed approach, while the presumed-PDF approach advances back the timing of events in approximately 0.05 ms.

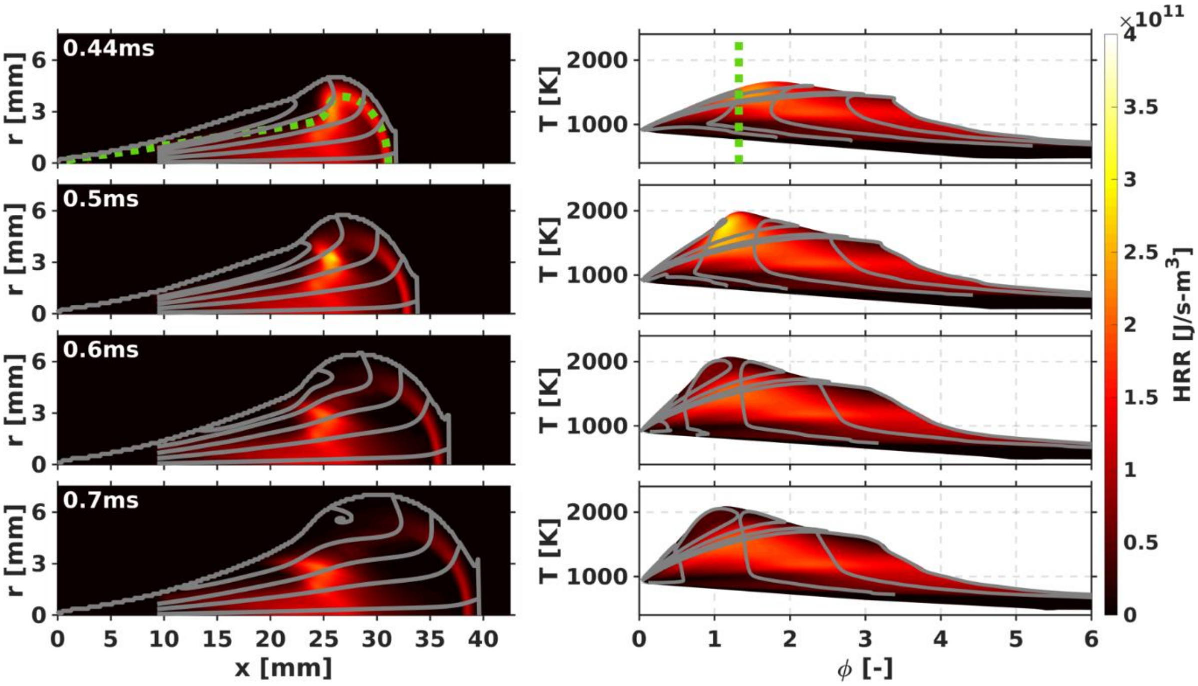

Figure 15. Time resolved local HRR in spatial coordinates (panels on the left) and in $\phi - T$ coordinates (panels on the right) for Spray A using the UFPV model. Dashed green line drawn at ϕ_{MR}.

The post-ignition sequence predicted by the UFPV model is shown in Figure 15. As already seen in the spatial representation of the HRR contour, the second-stage ignition takes place in a broader range of equivalence ratios and not just around ϕ_{MR}. Compared to WM results (Figure 12), where a defined steady low-temperature reaction zone was observed to be established upstream (10-20 mm) with another intermediate reaction layer close to the axis (around 22 mm), and the diffusion flame stabilization occurred by the propagation of two fronts along the stoichiometric surface, UFPV shows a much less intense low-temperature front over a wide spray region (15-25 mm), with the main heat release over the whole spray cross-section at around 20-25 mm. No transient front evolution can be observed around the stoichiometric surface, as was the case for the WM model. An important feature, however, is the very different appearance of the heat release at the LOL location, which will be analyzed in the next section.

4.3 Spray A quasi-steady state description

In spite of the almost quasi-steady appearance of the reacting spray at 0.7 ms in the previous section, the analysis of LOL for all modelling approaches is made for a later time, in which the spray head does not interact with the flame base. Figure 16 shows the contour of local HRR results for WM (top) and UFPV model (bottom). The spray radius is plotted with a gray solid line and the location of the stoichiometric equivalence ratio is plotted with a dashed green line. Both models predict heat as being release from three distinctive areas i.e. a low-temperature structure (zone I) at the flame base as a result of first-stage ignition, a diffusion flame front (zone III) around the stoichiometric equivalence ratio and an intermediate partially-premixed flame front (zone II) around the LOL location. While zones I and II are quite similar in both models, except for the fact that both fronts are narrower for the well-mixed model due to the absence of both sub-grid flamelet diffusion and presumed-PDFs integration, the location and appearance of zone II is a key difference between WM and UFPV predictions. Figure 17 shows a zoomed view of the local HRR contour around the area where LOL is stabilized including the well-mixed model, as well as the UFPV and UPFV-0 approaches. Mixing trajectories have been added (solid gray lines) to allow for the posterior link of spatial and $\phi - T$ coordinates. Blue "x" markers are plotted at the locations where OH mass fraction reach 14% of the maximum value in the spray following ECN guidelines for the location of LOL.

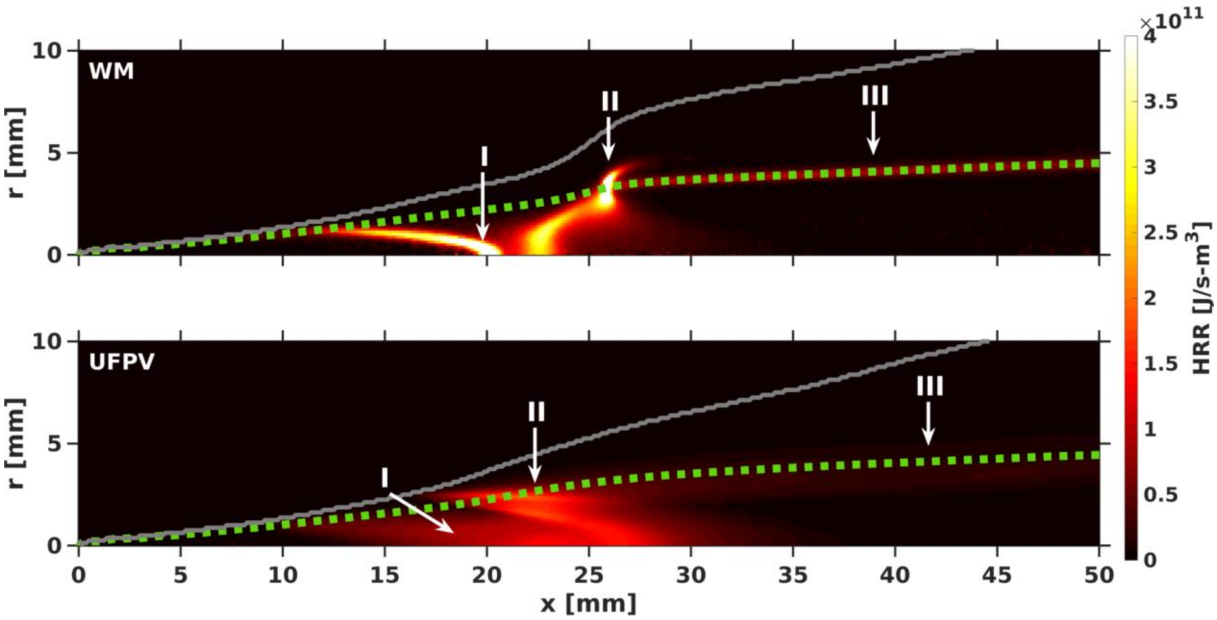

Figure 16. Local HRR contour at quasi-steady state for Spray A using WM (top) and UFPV model (bottom). Dashed green line drawn at $\phi = 1$.

From Figure 16 low and high-temperature heat release fronts (zones I and II) were shown to be spatially decoupled for the WM case. In contrast, the flame structure predicted by the UFPV model around the stabilized LOL position (Figure 17 bottom) shows how zones I and II are virtually merged. Compared to the well-mixed case, the introduction of χ_{ST} for UPFV-0 seems to contribute to the stabilization of zone I further downstream from the nozzle. This observation is consistent with a delayed temporal evolution of auto-ignition (comparing WM and UFPV-0 results) as described in the "Spray A auto-ignition sequence" section since high χ_{ST} values near the nozzle inhibit combustion. As for Zone II, sub-grid diffusion seems to contribute to the stabilization of the high-temperature front in both UFPV approaches closer to the nozzle as compared with WM results. Furthermore, the observed intermediate temperature zone close to the spray axis in the WM approach has a very similar shape in the UFPV-0 approach to the low-temperature one. The averaging role of the presumed-PDF approach is also seen, when comparing UFPV-0 and UFPV, in the sense that both low-temperature zones become eventually merged and the high-temperature heat release drops in intensity. All such features will be analyzed in $\phi - T$ coordinates in the following.

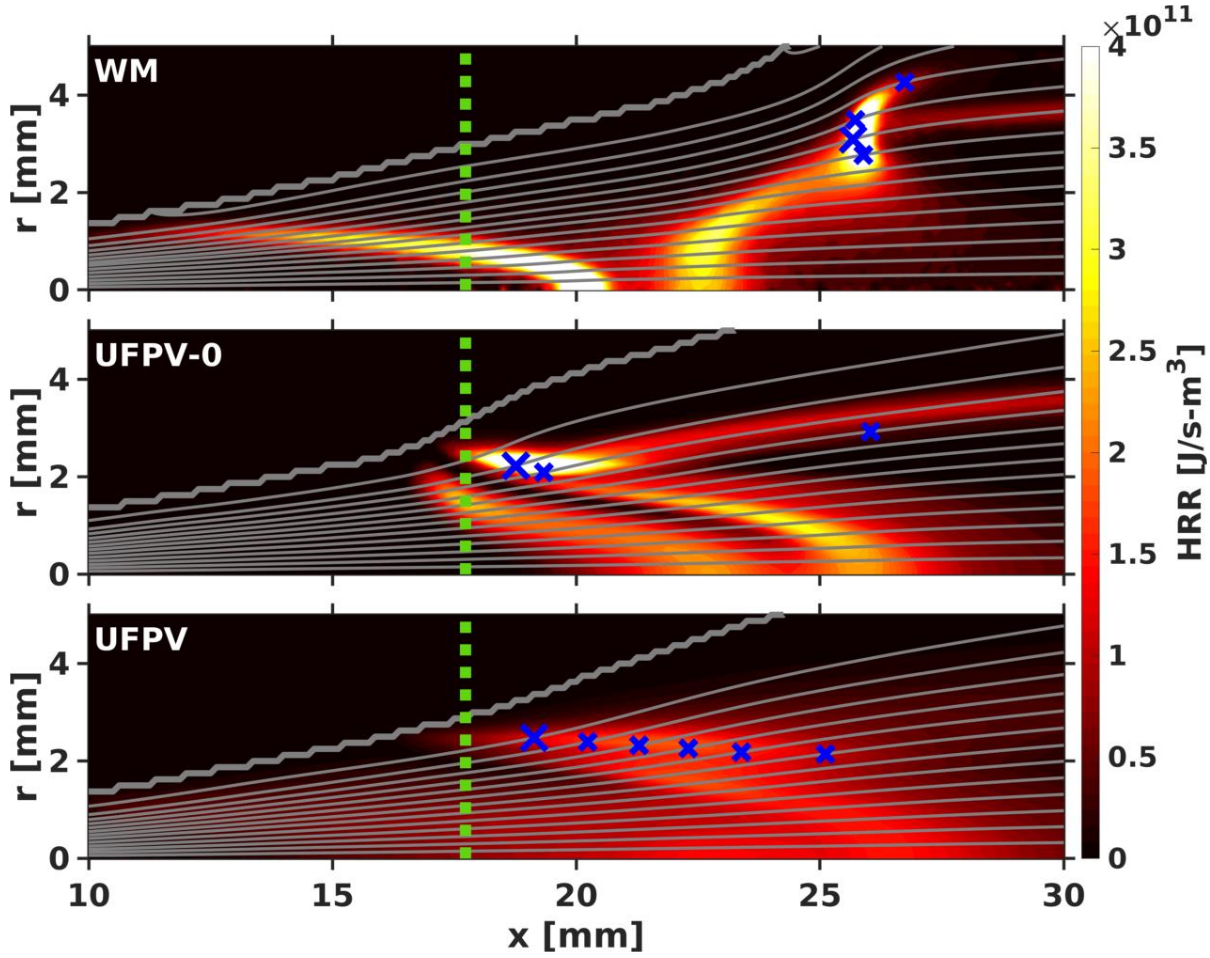

Figure 17. Local HRR contour at quasi-steady state near LOL location for Spray A using WM (top), UFPV-0 (middle) and UFPV model (bottom). Biggest blue "x" marker for mixing trajectory closest to predicted LOL (green dashed line).

With the inclusion of mixing trajectories, the path followed by a "conserved gas particle" can be depicted both in spatial and $\phi - T$ coordinates. Analysis of WM results (Figure 18 top) reveals how any "conserved gas particle" starts diluting almost along the inert adiabatic mixing trajectory, with a first noticeable increase in temperature as it passes through the low-temperature area (zone I in Figure 17 top). As already discussed, this initial flame front occurs at a similar temperature but at a different equivalence ratio for every single trajectory. Beyond zone I, two types of evolutions can be observed. For mixing trajectories closer to the axis, i.e. moving through richer equivalence ratio values, the also mentioned intermediate flame front can be observed at around 22-23 mm, and correspondingly at a temperature of around 1100 K. After that, no heat will be released along those trajectories until reaching the stoichiometric flame front. On the other hand, mixing trajectories reaching the stoichiometric flame front at around 25 mm directly run into the high-temperature heat release, and the intermediate temperature ignition is missing. This is probably due to the longer residence time associated with such radially displaced trajectories, which enables reaching high-temperature ignition for similar equivalence ratio values as those closer to the axis.

The inclusion of UFPV-0 results (Figure 18 middle) allows to isolate the effect of χ_{ST} in $\phi - T$ coordinates. As it was already mentioned when analyzing the effects of diffusion in spatial coordinates, there are two distinctive effects. On the one hand, when comparing the well-mixed results (no effect of χ_{ST}) with UFPV-0, it becomes clear that diffusion decreases reactivity for low-temperature chemistry (zone I in Figure 17) as the HRR is less intense in the zone below 1000 K, which becomes evident in the $\phi - T$ map. On the contrary, high-temperature heat release (upper part in the $\phi - T$ centered around $\phi = 1$) becomes wider in equivalence ratio and temperature ranges, especially towards the lean region. This effect speeds up the transition from low-temperature to high-temperature heat release with the consequent stabilization of LOL closer to the nozzle compared to WM results.

Finally, the description can also be carried-out for the UFPV model (Figure 18 bottom). In the same way as for spatial coordinates, the distinction among different flame fronts in the $\phi - T$ map is softened due to averaging. In this case, the low-temperature flame front occurs over a wide region upstream 20 mm for all trajectories, but the trends in the $\phi - T$ map does not depart substantially from the inert adiabatic mixing line. Instead of separated reaction regions around the LOL as for the WM model, UFPV shows a single high heat release zone starting radially at around 19 mm and which reaches the spray axis at around 26 mm. All mixing trajectories flow through this zone, shown by the steep increase in temperature in the $\phi - T$ map over a wide range of equivalence ratio values.

According to the previous differences in heat release zones, modelling approaches predict different locations for the LOL. On the one hand, the well-mixed approach predicts LOL to stabilize on the mixing trajectory passing through the most reactive spot in the high-temperature heat release zone close to the stoichiometric equivalence ratio. On the contrary, the UFPV model predicts LOL to stabilize at the lean high-temperature heat release zone. Furthermore, the UPFV-0 shows the underlying flame structure, with an intense stoichiometric combustion, which extends towards both the lean and rich sides, which may bring some remembrance with triple flame structures. Recent findings supported by DNS calculations under similar operating conditions show that LOL stabilization might take place at lean, stoichiometric or rich zones depending on the local flame topology,[44] but including triple flame effects.

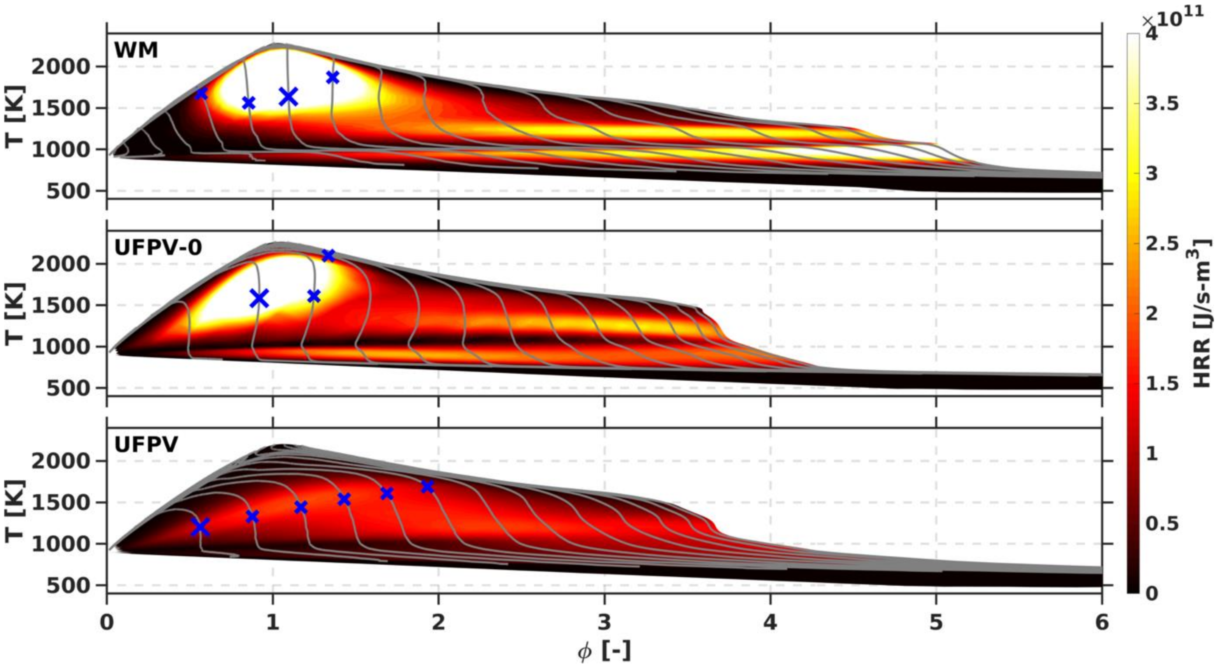

Figure 18. Local HRR contour at quasi-steady state in $\phi - T$ space for Spray A using WM (top), UFPV-0 (middle) and UFPV model (bottom). Biggest blue “x” marker for mixing trajectory closest to predicted LOL.

4.4 Spray D auto-ignition sequence

After a detailed description of the different modelling approaches for the Spray A case, the UFPV model is used to evaluate the influence of nozzle diameter in Diesel combustion following similar concepts. First, the auto-ignition sequence of Spray D will be analyzed. Local HRR contours are plotted in Figure 19 (along with the spray radius and the iso-contour of ϕ_{MR}) for several timings up to the ID timing at 0.53 ms.

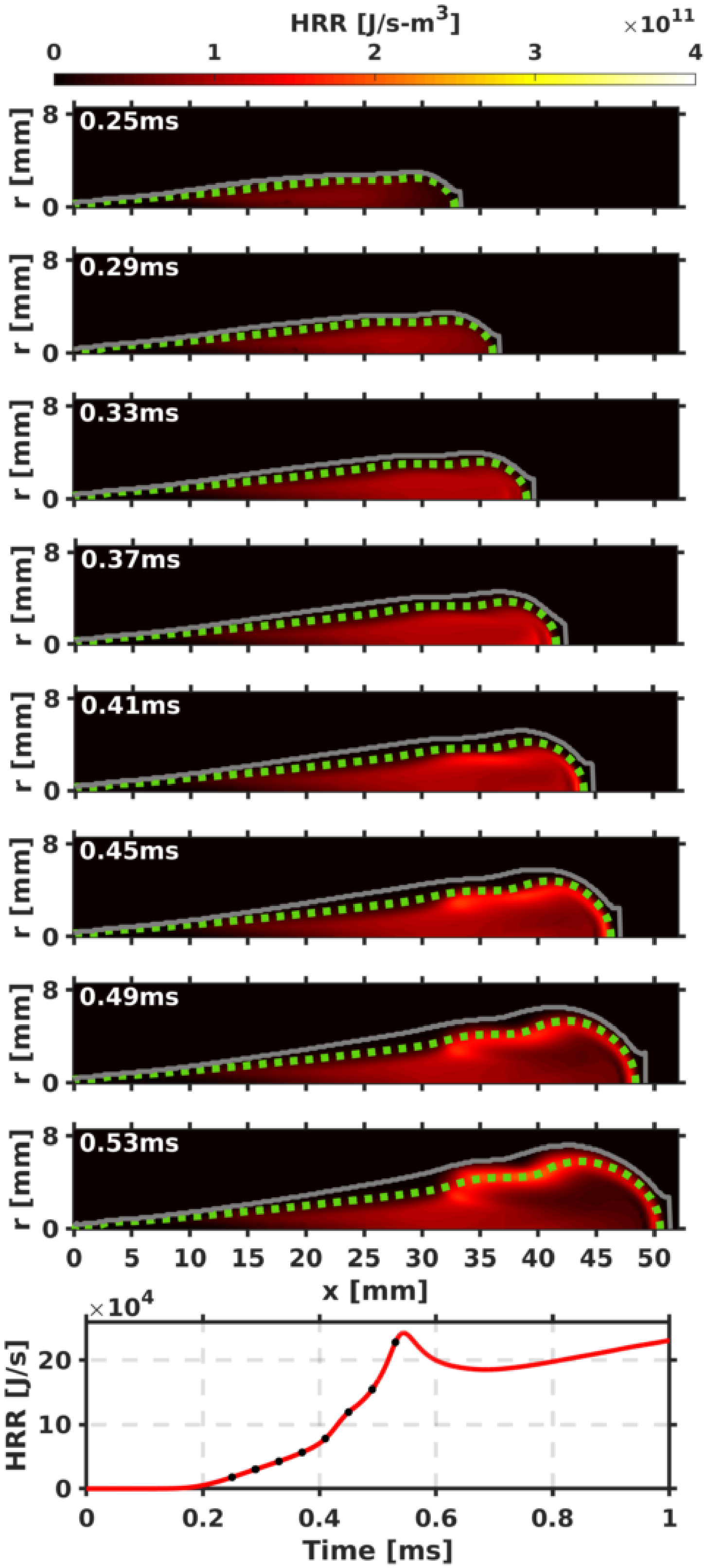

Figure 19. Time and spatially resolved local HRR for Spray D using the UFPV model. Dashed green line drawn at ϕ_{MR}. Bottom plot shows the integrated HRR, where markers indicate the timings of the local HRR contours.

The sequence depicted in Figure 19 evidences that both nozzles (see Figure 14 for Spray A results) share similar features on how the flame is established i.e. a cool flame originated at the spray radial periphery (in a broader range of mixtures not limited to ϕ_{MR}), a quasi-homogeneous state of heat release (at 0.32 ms for Spray A and at 0.37 ms for Spray D) and finally a decrease in the HRR prior to second-stage ignition taking place at the spray radial periphery (at 0.44 ms for Spray A and at 0.53 ms for Spray D). The location of second-stage ignition for Spray A is seen to occur closer to the spray tip compared to Spray D, where this occurs essentially upstream of the spray tip front. Higher χ_{ST} values reported above for Spray A play an important role in the spatial shift of ignition location compared to the larger nozzle. Differences in ignition location among nozzles are consistent with those reported in the literature from experimental observations by Pastor et al.[4]

In agreement with previously discussed longer residence time for Spray D nozzle, a slower progression of the auto-ignition sequence is expected compared to spray A, as it takes more time to reach reactive ignitable mixtures, which might be compensated to some extent by the lower χ_{ST} values of the larger nozzle. From simulation results, the whole ignition sequence is seen to be already delayed from the initial low-temperature stages, and eventually Spray D ignites 94 μs later compared to Spray A. In that same direction, from experimental observations Spray D high-temperature ignition occurs 137 μs later compared to Spray A. These differences are consistent with a slower mixing process as previously described in the “Validation of the computational setup” section. Aside from timing, the general development of the ignition sequence on Spray D occurs at richer equivalence ratio values. The longer residence time for Spray D enables the ignition of richer mixtures less favorable from the point of view of temperature and equivalence ratio. This observation will be further analyzed in the next section.

4.5 Spray D quasi-steady state description

After ignition, both nozzles also share similar heat release zones at quasi-steady state. The previously observed zones I, II and III for Spray A (Figure 16 bottom) are also reproduced in Spray D, resulting in a similar flame structure, with an upstream location occurring at richer mixtures for the larger nozzle following the auto-ignition comparison. A closer look at zone II in Figure 20, where LOL is stabilized, confirms the similarity of Spray A and Spray D flame structure. The use of normalized coordinates already points at a stabilization of the flame base at a richer location in Spray D compared to Spray A.

In Figure 20, mixing trajectories are superimposed onto the local HRR contour, and in Figure 21 the corresonding $\phi - T$ maps are shown. The positions where the mixing trajectories go above the contour of the 14% of the maximum OH mass fraction are highlighted with blue “x” markers. As previously observed for Spray A the closest point to the nozzle, which defines the LOL value in both cases, occur in the most radially displaced trajectory, i.e. at lean conditions.

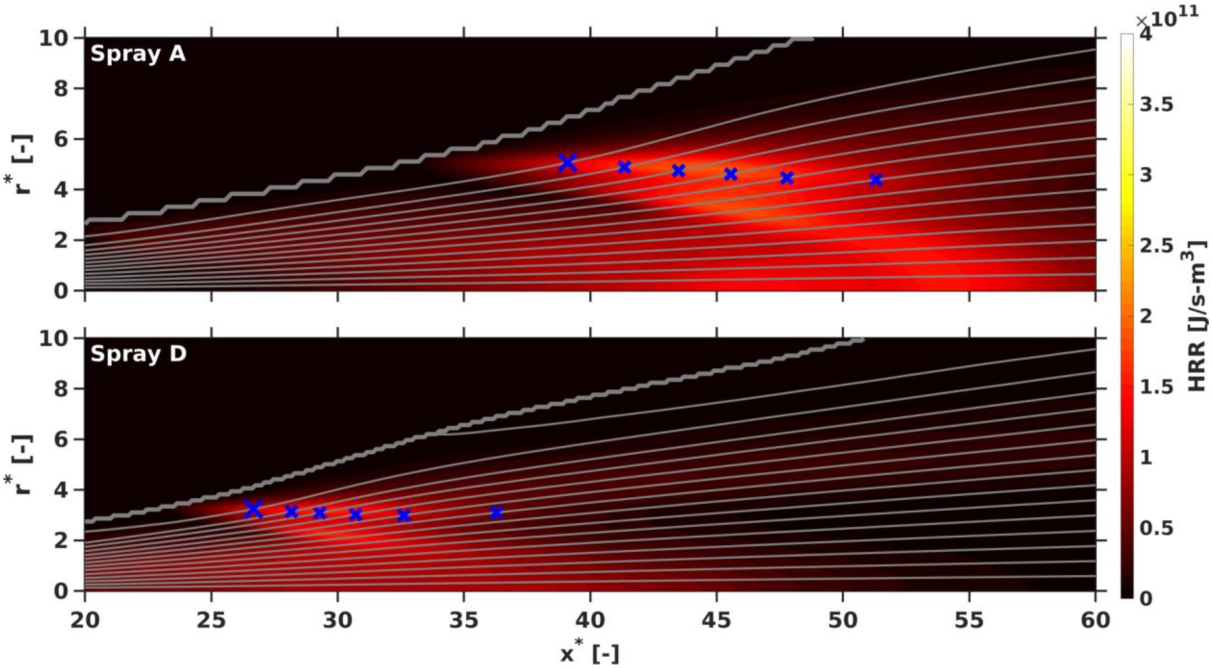

Figure 20. Local HRR contour at quasi-steady state near LOL location for Spray A (top) and Spray D (bottom) using the UFPV model. Spatial coordinates have been normalized by d_{eq}. Biggest blue "x" marker for mixing trajectory closest to predicted LOL.

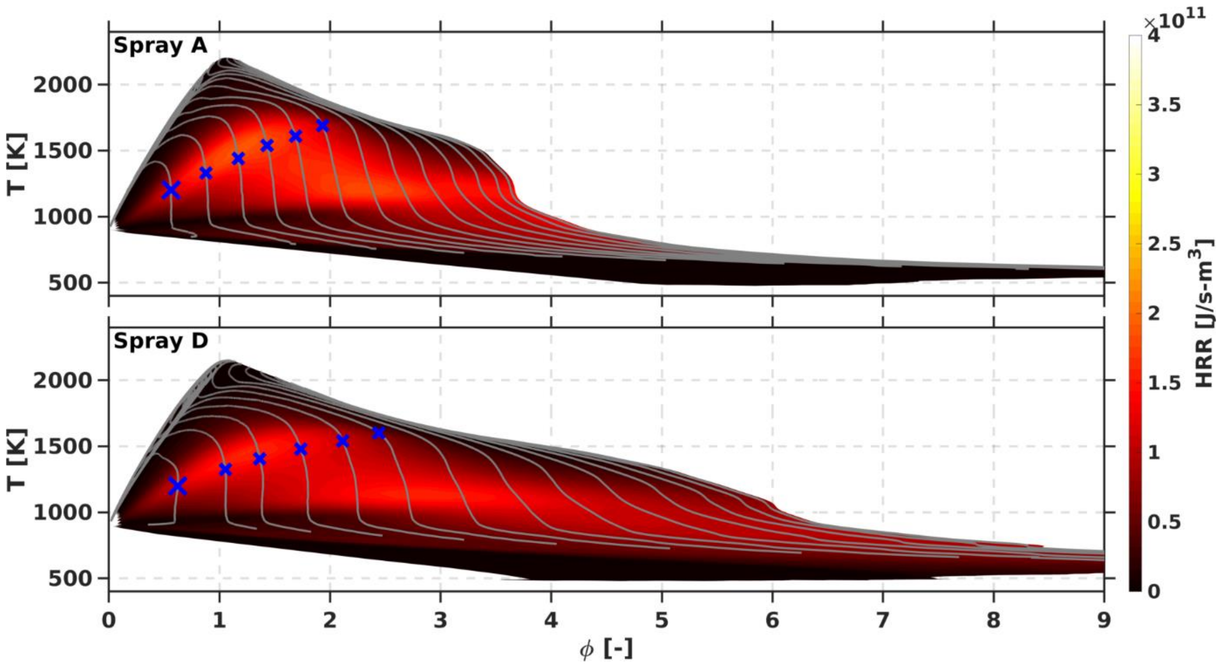

Figure 21. Local HRR contour at quasi-steady state in ϕ-T space for Spray A (top) and Spray D (bottom) using the UFPV model. Biggest blue "x" marker for mixing trajectory closest to predicted LOL.

Despite evident similarities between the two nozzles studied in this work, a major distinction has already been mentioned, i.e. both ignition and lift-off length stabilization occur in more fuel-rich mixtures in Spray D as compared to Spray A. This observation is sustained by a slower mixing process with consequent longer residence time for Spray D. In $\phi - T$ coordinates Spray D richer combustion is evidenced by the presence of mixing trajectories increasing in temperature for $\phi > 4$, which does not happen for Spray A. Such trajectories are the ones closest to the axis, where the scalar dissipation rate is lower, which also contributes to the possibility of reaction to progress in richer equivalence ratio zones. On the other hand, trajectories linked to the LOL stabilization (blue markers in Figure 20 and Figure 21) reach the lift-off limit at similar equivalence ratio and temperature values for both nozzles. However, the different development of the mixing process in terms of spatial distribution and local residence time results in different spatial locations for this high-temperature zone between both nozzles.

5 Conclusions

The effect of nozzle orifice diameter on Diesel combustion has been studied. Spray A and Spray D from the ECN have been modeled and validated under nonreacting and reacting conditions using CFD. For the nonreacting condition, the applicability of the mixing trajectory concept has been assessed for both nozzles along with the concept of local residence time. For the reacting condition, commonly made assumptions for TCI have been evaluated for Spray A. For this purpose, auto-ignition sequence and quasi-steady state results from the WM and the UFPV models have been analyzed. Finally, a comparison of auto-ignition and quasi-steady state results of the two nozzles has been made.

Main conclusions from this study can be summarized in the following:

- Under the nonreacting condition, local residence time has been quantified for both nozzles. Results show that it increases at locations farther away from the nozzle both in axial and radial directions. This observation is consistent with the location at which main ignition is observed to take place. Both WM and UFPV models predict main ignition as taking place near the spray periphery. At his location in the spray two observations should be emphasized. On the one hand, a “conserved gas particle” has already diluted as it follows its mixing trajectory. On the other hand, local residence time is high enough as to let chemistry progress.
- The reduction of the nozzle diameter promotes faster mixing. Under the nonreacting condition the time spent at a given ϕ is shorter in Spray A compared to Spray D. Taking into account the description of the spray as a set of trajectories where mixture fraction is progressively diluting, this means that the faster mixing for Spray A enables reaching

ignitable equivalence ratio values earlier. Therefore, the shorter ID time for the smaller nozzle is consistent with shorter residence time.

- For the reacting Spray A condition both WM and UFPV models predict similar global steps leading to main ignition. The main difference is related to the spatial width of the area that characterizes this event. WM results show main ignition occurring at a narrow range of mixtures centered around ϕ_{MR}. On the contrary, UFPV results show how main ignition takes place on a broader range of mixtures.
- At quasi-steady state the predicted flame structure for Spray A is remarkably different among the two combustion models. The scalar dissipation rate (only accounted for in the UFPV model) seems to shift further downstream the low-temperature heat release zone compared to WM results. The downstream shift is consistent with high χ_{ST} near the nozzle. On the high-temperature heat release zone, χ_{ST} is observed to play an opposite role contributing to the stabilization of the LOL closer to the nozzle compared to WM results. The comparison of UFPV and the intermediate UFPV-0 model, considering the flamelet sub-grid structure but not the presumed-PDF integration, evidences that one of the reasons for the wider spatial location of reaction zones is the averaging of laminar flamelets, smoothing the gradients within the reacting zones of the spray.
- UFPV results for Spray A and Spray D show a similar ignition sequence for both nozzles. Faster mixing and higher χ_{ST} values for Spray A cause main ignition to occur closer to the spray head compared so Spray D where main ignition occurs closer to the spray radial periphery.
- In spatial coordinates, both Spray A and Spray D share a similar flame structure at quasi-steady state. In $\phi - T$ space Spray D is characterized by richer mixtures being able to ignite. A slower mixing process, thus longer residence time, allow richer mixtures to ignite in the larger nozzle close to the axis, with lower scalar dissipation rate also contributing to this ignition capability.

Acknowledgements

This work was partially funded by the Government of Spain through the CHEST Project (TRA2017-89139-C2-1-R) and by Universitat Politècnica de València through the Programa de Ayudas de Investigación y Desarrollo (PAID-01-16). CONVERGENT SCIENCE Inc support is greatly acknowledged. The authors also want to express their gratitude to Dr. Bertrand Naud from CIEMAT for the development of the flamelet solver used in this work.

Appendix A. Mixing trajectories

In problems of momentum transfer, fluid flow is usually analyzed in terms of streamlines, i.e. lines describing the convective flow movement. In cases where species are also transported by means of convection and diffusion, both terms have to be accounted when tracking species. Assuming azimuthal symmetry, generally occurring in single spray cases such as the one under investigation, so-called “mixing trajectories” can be obtained by integration of the equation:

$$\frac{dx}{u + u_{dif}} = \frac{dr}{v + v_{dif}} \tag{11}$$

In Equation (11), u and v denote the convective components of the velocity field, while u_{dif} and v_{dif} allow for the consideration of the transport flow induced by the diffusion of mixture fraction. Following a RANS approach for a spray at high Reynolds number, turbulent diffusion is assumed to be much more important than the laminar one. Therefore, diffusive components[45] are defined in an analogue way to a Fick’s diffusion law (where the diffusion flux can be written as $gf = \rho Z v_{dif}$), according to:

$$u_{dif} = -\frac{D_t}{Z}\frac{\partial Z}{\partial x} \tag{12}$$

$$v_{dif} = -\frac{D_t}{Z}\frac{\partial Z}{\partial r} \tag{13}$$

where diffusivity has been assumed equal to the RANS turbulent one, calculated from turbulent viscosity via a unity Schmidt turbulent number, which has been imposed in the CFD calculations. Therefore, the diffusion coefficient in Equation (12) and Equation (13) is calculated as $D_t = C_\mu \, \kappa^2/\varepsilon$ with $C_\mu = 0.09$.

The mixing field, described by Z, is shown in Figure 22 for both Spray A and Spray D at several time instants after start of injection. The contour of the spray is delimited by the spray radius marked at the locations where Z is 1% of the value on the spray axis. Finally, mixing trajectories are also plotted on the contour plots in Figure 22. These are calculated downstream of the liquid length to avoid any effect induced by Lagrangian parcels, as the mixing trajectories are mainly an Eulerian concept.

Time development of mixing trajectories agrees with the general evolution of the spray, where a transient zone progresses at the tip of the spray, behind which a quasi-steady flow is established. In this sense, mixing trajectories are almost straight lines with a direction that barely changes until reaching around 70-80% of the tip penetration. Transient structures can be observed at the furthest radial locations around the tip of the spray.

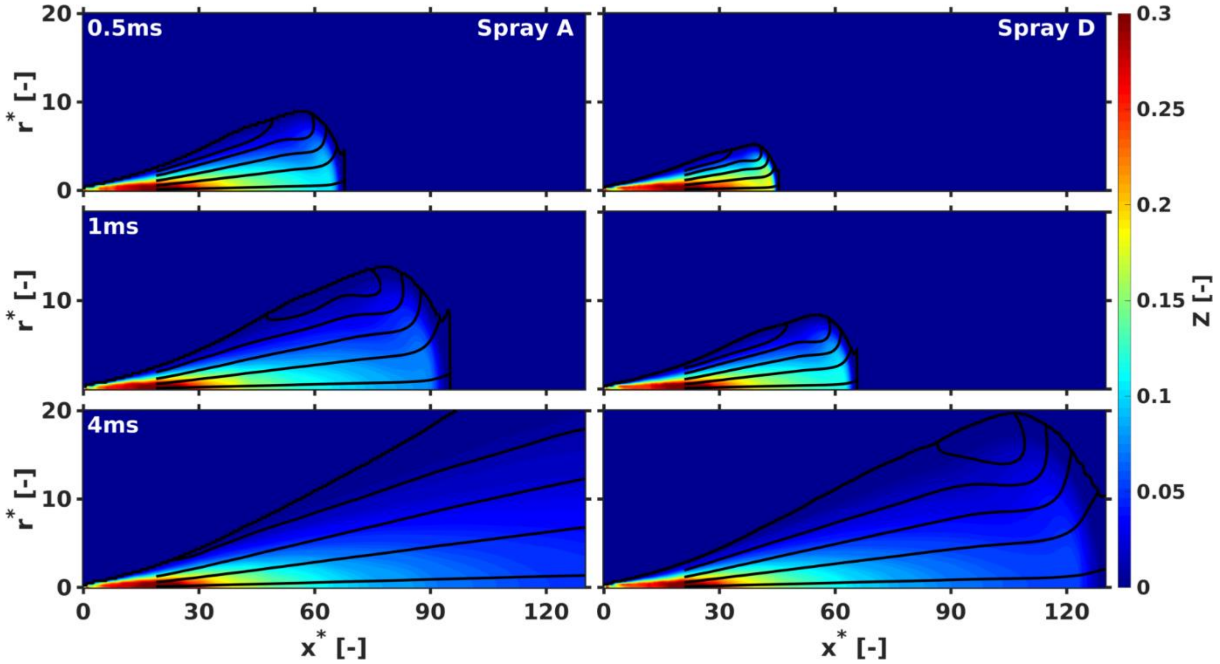

Figure 22. Mixture fraction field and mixing trajectories for Spray A (left) and Spray D (right).

It is also worth mentioning that by normalizing the axial and radial coordinates, at any given point defined by (x^*, r^*) the same Z value for both nozzles is reached. This observation is confirmed as trajectories for both nozzles start at $x^* \cong 20\ d_{eq}$ indicating that both nozzles have a similar saturation Z value. This is also expected since saturation Z depends on the fuel, fuel temperature and ambient temperature and pressure.

Appendix B. Extended study of global combustion parameters

As described in the "Computational setup" section the chemical mechanism by Yao et al.[34] has been used in this work to describe the oxidation of n-dodecane. Figure 23 shows the predicted values for ignition delay and lift-off length for the chemical mechanisms by Yao et al.[34] (as presented in Figure 10) and Narayanaswamy et al.[46] This last chemical mechanism comprising 257 species and 1521 reactions is also used to describe the oxidation of n-dodecane. Despite differences in the predicted values for ID and LOL, the trend between nozzles (i.e. longer ID and LOL for Spray D compared to Spray A) remains the same regardless of the chemical mechanism choice for both WM and UFPV models. This observation shows that the main conclusions in this work concerning the effect of nozzle diameter on Diesel combustion hold valid independently of the chemical mechanism used.

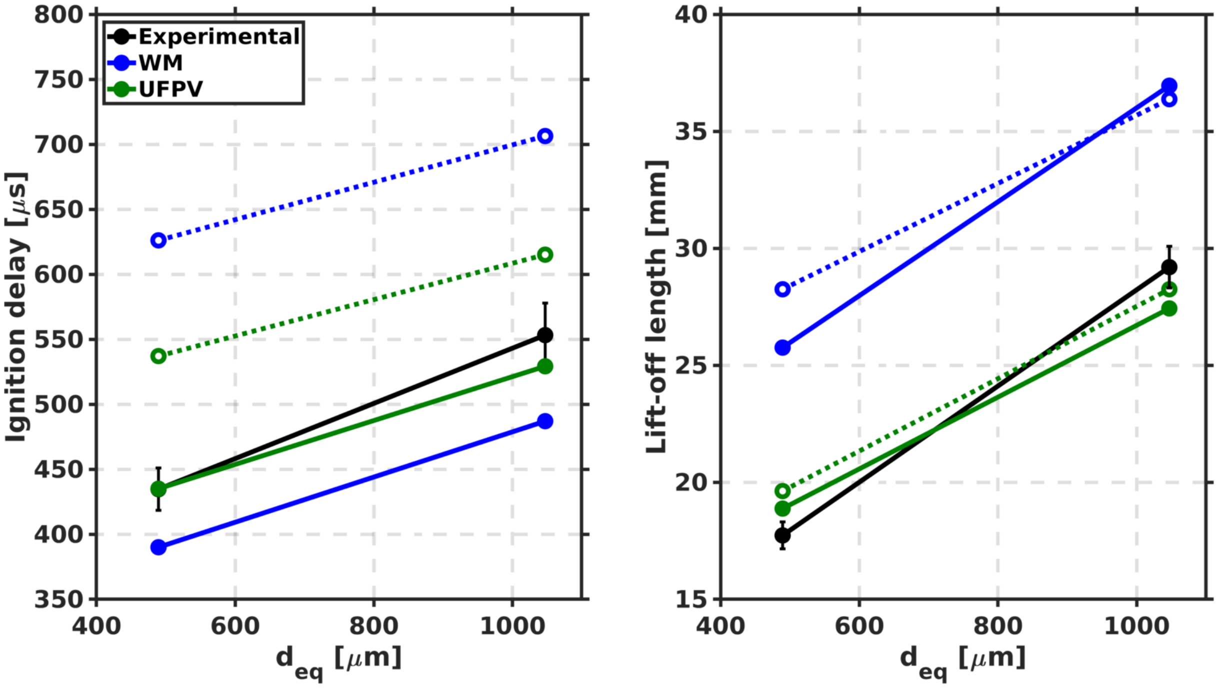

Figure 23. Ignition delay and lift-off length for Spray A and Spray D using the chemical mechanism by Yao et al.[34] (solid line) and Narayanaswamy et al.[46] (dashed line).

Finally, Figure 24 and Figure 25 depict the Spray A auto-ignition sequence for the Narayanaswamy et al.[46] chemical mechanism using the WM and the UFPV models, respectively. The figures show the local HRR contour with the spray radius and the most reactive equivalence ratio iso-contour ($\phi_{MR} = 1.39$). Despite differences in the maximum HRR level reached, both results share the same auto-ignition characteristics highlighted for the chemical mechanism by Yao et al.[34] in Figure 11 for the WM model and in Figure 14 for the UFPV model.

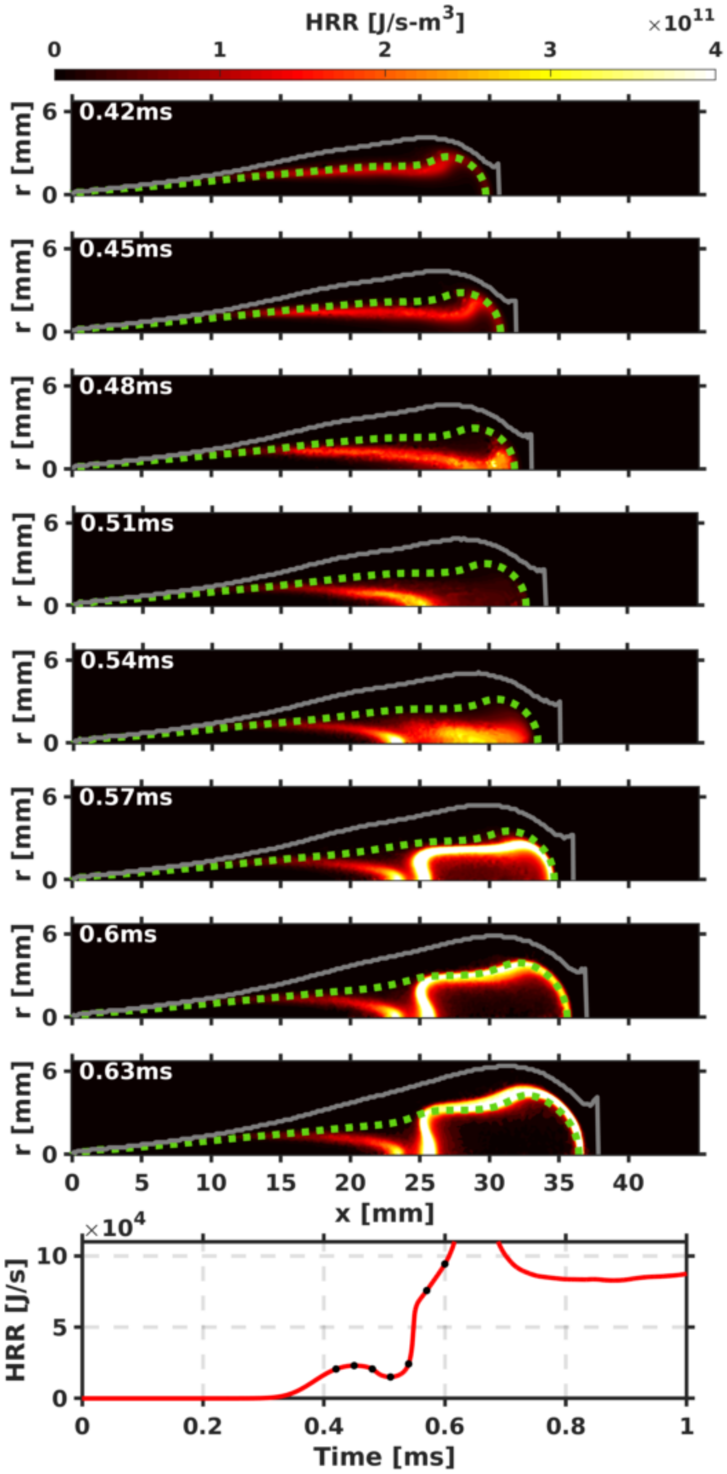

Figure 24. Time and spatially resolved local HRR for Spray A using the WM model and the Narayanaswamy et al.[46] chemical mechanism. Dashed green line drawn at ϕ_{MR}. Bottom plot shows the integrated HRR, where markers indicate the timings of the local HRR contours.

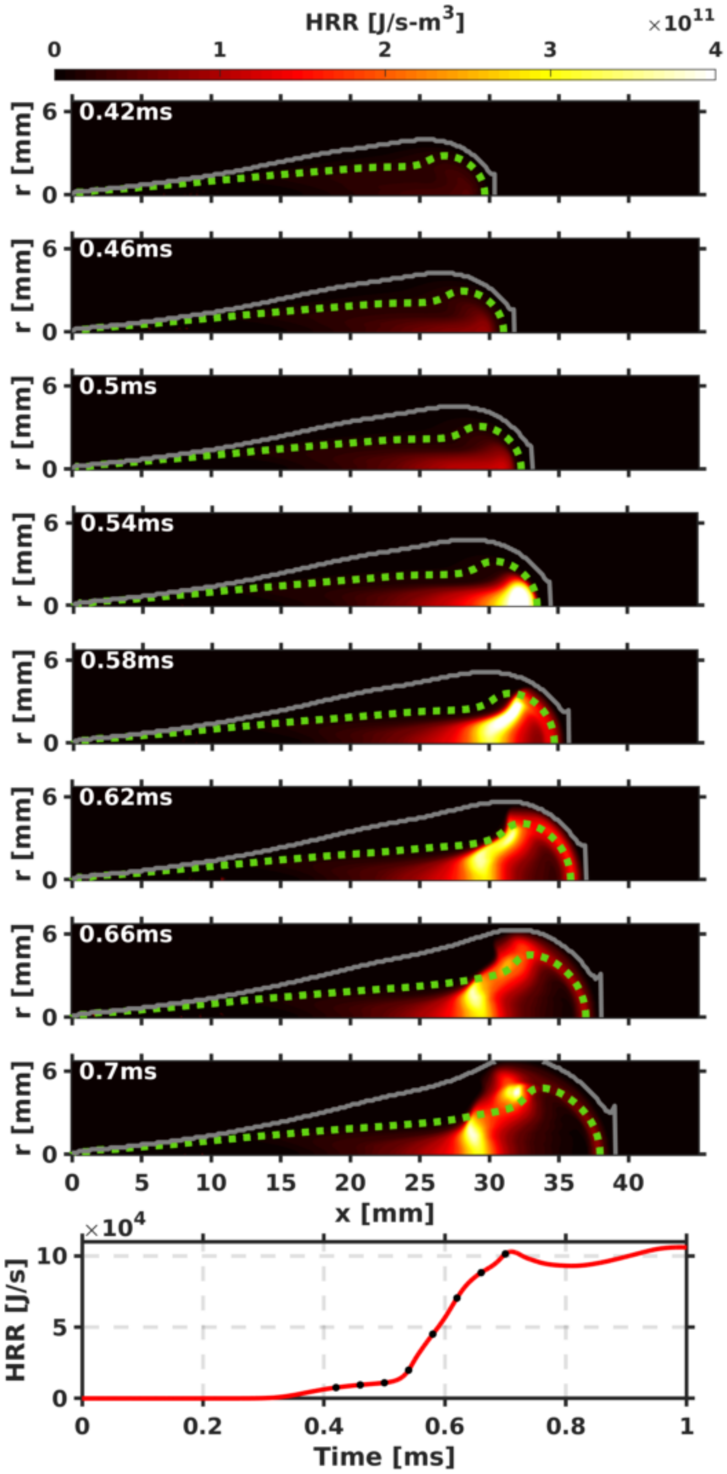

Figure 25. Time and spatially resolved local HRR for Spray A using the UFPV model and the Narayanaswamy et al.[46] chemical mechanism. Dashed green line drawn at ϕ_{MR}. Bottom plot shows the integrated HRR, where markers indicate the timings of the local HRR contours.

References

1. Pickett LM, Siebers DL. An investigation of diesel soot formation processes using micro-orifices. *Proceedings of the Combustion Institute* 2002; 29: 655–662.

2. Pickett LM, Siebers DL. Orifice Diameter Effects on Diesel Fuel Jet Flame Structure. *Journal of Engineering for Gas Turbines and Power* 2005; 127: 187.

3. Du C, Andersson S, Andersson M. Two-dimensional measurements of soot in a turbulent diffusion diesel flame: the effects of injection pressure, nozzle orifice diameter, and gas density. *Combustion Science and Technology* 2018; 190: 1659–1688.

4. Pastor JV, Garcia-Oliver JM, Garcia A, et al. An Experimental Investigation on Spray Mixing and Combustion Characteristics for Spray C/D Nozzles in a Constant Pressure Vessel. In: *International Powertrains, Fuels & Lubricants Meeting*. DOI: 10.4271/2018-01-1783.

5. Ishibashi R, Tsuru D. An optical investigation of combustion process of a direct high-pressure injection of natural gas. *Journal of Marine Science and Technology* 2017; 22: 447–458.

6. Pang KM, Jangi M, Bai X-S, et al. Effects of Nozzle Diameter on Diesel Spray Flames: A numerical study using an Eulerian Stochastic Field Method. *Energy Procedia* 2017; 142: 1028–1033.

7. Engine Combustion Network, https://ecn.sandia.gov/.

8. Idicheria CA, Pickett LM. Quantitative Mixing Measurements in a Vaporizing Diesel Spray by Rayleigh Imaging. In: *SAE Technical Paper*, pp. 2007-01–0647.

9. Pickett LM, Manin J, Genzale CL, et al. Relationship Between Diesel Fuel Spray Vapor Penetration/Dispersion and Local Fuel Mixture Fraction. *SAE Int J Engines* 2011; 4: 764–799.

10. García-Oliver JM, Malbec L-M, Toda HB, et al. A study on the interaction between local flow and flame structure for mixing-controlled Diesel sprays. *Combustion and Flame* 2017; 179: 157–171.

11. Dahms RN, Paczko GA, Skeen SA, et al. Understanding the ignition mechanism of high-pressure spray flames. *Proceedings of the Combustion Institute* 2017; 36: 2615–2623.

12. Gimeno J, Martí-Aldaraví P, Carreres M, et al. Effect of the nozzle holder on injected fuel temperature for experimental test rigs and its influence on diesel sprays. *International Journal of Engine Research* 2018; 19: 374–389.

13. Matusik KE, Duke DJ, Kastengren AL, et al. High-resolution X-ray tomography of Engine Combustion Network diesel injectors. *International Journal of Engine Research* 2018; 19: 963–976.

14. Tsang C-W, Kuo C-W, Trujillo M, et al. Evaluation and validation of large-eddy simulation sub-grid spray dispersion models using high-fidelity volume-of-fluid simulation data and engine combustion network experimental data. *International Journal of Engine Research* 2018; 146808741877221.

15. Owoyele O, Kundu P, Ameen MM, et al. Application of deep artificial neural networks to multi-dimensional flamelet libraries and spray flames. *International Journal of Engine Research* 2019; 146808741983777.

16. Pandurangi SS, Bolla M, Wright YM, et al. Onset and progression of soot in high-pressure n-dodecane sprays under diesel engine conditions. *International Journal of Engine Research* 2017; 18: 436–452.

17. Aubagnac-Karkar D, Michel J-B, Colin O, et al. Combustion and soot modelling of a high-pressure and high-temperature Dodecane spray. *International Journal of Engine Research* 2018; 19: 434–448.

18. Ihme M, Ma PC, Bravo L. Large eddy simulations of diesel-fuel injection and auto-ignition at transcritical conditions. *International Journal of Engine Research* 2019; 20: 58–68.

19. Yue Z, Reitz RD. An equilibrium phase spray model for high-pressure fuel injection and engine combustion simulations. *International Journal of Engine Research* 2017; 20: 203–215.

20. Lackmann T, Nygren A, Karlsson A, et al. Investigation of turbulence–chemistry interactions in a heavy-duty diesel engine with a representative interactive linear eddy model. *International Journal of Engine Research* 2018; 1468087418812319.

21. Bhattacharjee S, Haworth DC. Simulations of transient n-heptane and n-dodecane spray flames under engine-relevant conditions using a transported PDF method. *Combustion and Flame* 2013; 160: 2083–2102.

22. Pei Y, Hawkes ER, Kook S. Transported probability density function modelling of the vapour phase of an n-heptane jet at diesel engine conditions. *Proceedings of the Combustion Institute* 2013; 34: 3039–3047.

23. Pang KM, Jangi M, Bai X-S, et al. Modelling of diesel spray flames under engine-like conditions using an accelerated Eulerian Stochastic Field method. *Combustion and Flame* 2018; 193: 363–383.

24. D'Errico G, Lucchini T, Contino F, et al. Comparison of well-mixed and multiple representative interactive flamelet approaches for diesel spray combustion modelling. *Combustion Theory and Modelling* 2014; 18: 65–88.

25. Kosters A, Karlsson A, Oevermann M, et al. RANS predictions of flame lift-off: comparison of a reactor and a flamelet combustion model to the well stirred approach. *Combustion Theory and Modelling*; 25.

26. Lucchini T, D'Errico G, Onorati A, et al. Modeling Non-Premixed Combustion Using Tabulated Kinetics and Different Flame Structure Assumptions. *SAE International Journal of Engines* 2017; 10: 593–607.

27. Singh S, Reitz RD, Musculus MPB. Comparison of the Characteristic Time (CTC), Representative Interactive Flamelet (RIF), and Direct Integration with Detailed Chemistry Combustion Models against Optical Diagnostic Data for Multi-Mode Combustion in a Heavy-Duty DI Diesel Engine. In: *SAE Technical Paper*. DOI: 10.4271/2006-01-0055.

28. Lucchini T, D'Errico G, Cerri T, et al. Experimental Validation of Combustion Models for Diesel Engines Based on Tabulated Kinetics in a Wide Range of Operating Conditions. In: *13th International Conference on Engines & Vehicles*. DOI: 10.4271/2017-24-0029.

29. Pal P, Keum S, Im HG. Assessment of flamelet versus multi-zone combustion modeling approaches for stratified-charge compression ignition engines. *International Journal of Engine Research* 2016; 17: 280–290.

30. CONVERGE CFD Software, https://convergecfd.com.

31. POPE SB. An explanation of the turbulent round-jet/plane-jet anomaly. *AIAA Journal* 1978; 16: 279–281.

32. Novella R, García A, Pastor JM, et al. The role of detailed chemical kinetics on CFD diesel spray ignition and combustion modelling. *Mathematical and Computer Modelling* 2011; 54: 1706–1719.

33. *CONVERGE Manual*. Convergent Science, May 2016.

34. Yao T, Pei Y, Zhong B-J, et al. A compact skeletal mechanism for n -dodecane with optimized semi-global low-temperature chemistry for diesel engine simulations. *Fuel* 2017; 191: 339–349.

35. Perez E. *Application of a flamelet-based combustion model to diesel-like reacting sprays*. Universitat Politècnica de València, 2019.

36. Senecal PK, Pomraning E, Richards KJ, et al. Multi-Dimensional Modeling of Direct-Injection Diesel Spray Liquid Length and Flam Lift-off Length using CFD an Parallel Detailed Chemistry. In: *SAE Technical Paper*. 2003, pp. 1331–1351.

37. Williams FA. Recent Advances in Theoretical Descriptions of Turbulent Diffusion Flames. In: Murthy SNB (ed) *Turbulent Mixing in Nonreactive and Reactive Flows*. Boston, MA: Springer New York, pp. 189–208.

38. Peters N. *Turbulent Combustion*. Cambridge University Press. DOI: 10.1017/CBO9780511612701.

39. Poinsot T, Veynante D. *Theoretical and numerical combustion*. RT Edwards, Inc., 2005.

40. Naud B, Novella R, Pastor JM, et al. RANS modelling of a lifted H 2 /N 2 flame using an unsteady flamelet progress variable approach with presumed PDF. *Combustion and Flame* 2015; 162: 893–906.

41. Payri R, García-Oliver JM, Xuan T, et al. A study on diesel spray tip penetration and radial expansion under reacting conditions. *Applied Thermal Engineering* 2015; 90: 619–629.

42. Kahila H, Wehrfritz A, Kaario O, et al. Large-eddy simulation on the influence of injection pressure in reacting Spray A. *Combustion and Flame* 2018; 191: 142–159.

43. Pang KM, Jangi M, Bai X-S, et al. Effects of ambient pressure on ignition and flame characteristics in diesel spray combustion. *Fuel* 2019; 237: 676–685.

44. Tagliante F, Poinsot T, Pickett LM, et al. A conceptual model of the flame stabilization mechanisms for a lifted Diesel-type flame based on Direct Numerical Simulation and experiments. *Combustion and Flame* 2019; 201: 65–77.

45. Kuo K. *Principles of Combustion*. New York: John Wiley & Sons, Inc, 1986.

46. Narayanaswamy K, Pepiot P, Pitsch H. A chemical mechanism for low to high temperature oxidation of n-dodecane as a component of transportation fuel surrogates. *Combustion and Flame* 2014; 161: 866–884.